JOURNAL OF GEOPHYSICAL RESEARCH, VOL. 112, F04004, doi:10.1029/2007JF000772, 2007

Characteristics of steady state fluvial topography above fault-bend folds

Scott R. Miller,[1] Rudy L. Slingerland,[1] and Eric Kirby[1]

Received 7 February 2007; revised 15 June 2007; accepted 26 July 2007; published 31 October 2007.

[1] In steady state convergent orogens, erosion balances lateral as well as vertical bedrock motions. For simple geometrical reasons, the difference between the total steady state erosion flux and its vertical component is up to 30% for typical fluvial slopes and bedrock streamline inclinations, suggesting that lateral advection is also likely to be expressed topographically. In order to understand these geomorphologic consequences, we focus on steady state topography developed on active fault-bend folds. First, we derive an analytical solution for the slopes of detachment-limited streams that incorporates lateral advection. Next, we conduct experiments using a numerical two-dimensional landscape evolution model (Channel-Hillslope Integrated Landscape Development model (CHILD)) incorporating linear diffusion on hillslopes and detachment-limited stream channel incision above a fault-bend fold. The concavity and steepness indices of steady state long profiles are functions of bedrock velocity magnitude and direction, streamflow direction, and fluvial erosivity. Asymmetry of mountain range profiles varies as a function of fluvial erosivity or bedrock velocity only if we account for the lateral velocity component. This asymmetry is equally sensitive to this lateral component, fluvial incision, and hillslope diffusion. However, the effect of diffusion on drainage divide position is significant only at high diffusivities, short length scales, low bedrock advection rates, or relatively low fluvial erosivity. Thus in most mountain ranges and fault blocks, drainage divide migration is expected to be dictated by stream channel erosion. Model results are shown to be consistent with topography in the Siwalik Hills, Nepal, which overlie fault-bend folds produced above the frontal fault systems in the Himalayan foreland.

Citation: Miller, S. R., R. L. Slingerland, and E. Kirby (2007), Characteristics of steady state fluvial topography above fault-bend folds, *J. Geophys. Res.*, *112*, F04004, doi:10.1029/2007JF000772.

1. Motivation

[2] Much recent interest in tectonic geomorphology has arisen from the basic thesis that we can determine rates and styles of deformation from measurements of landscape form [see *Burbank and Anderson*, 2001, and references therein]. In particular, stream profile shape is argued to be a first-order predictor of rock uplift rate [e.g., *Lague et al.*, 2000; *Snyder et al.*, 2000; *Kirby and Whipple*, 2001; *Lavé and Avouac*, 2001; *Wobus et al.*, 2006a] and the shapes of landscapes have been quantitatively shown to reflect surface, climate, and lithospheric processes and their feedbacks in tectonically active settings [e.g., *Willett*, 1999; *Beaumont et al.*, 2001; *Willett et al.*, 2006].

[3] Despite these advances, conceptual and mathematical relationships between surface processes and mountain building have often been simplified to competitions between rock uplift (the vertical displacement of bedrock relative to a fixed datum such as the geoid) and erosion [*England and Molnar*, 1990]. However, field geologists, geodesists, and geodynamic modelers alike agree that the motion of bedrock within convergent orogens commonly includes large lateral or horizontal components. On both observational and theoretical grounds it is clear that mountain ranges and their structures, ranging from fold-and-thrust belts [e.g., *Suppe*, 1983; *Lavé and Avouac*, 2000] to small orogens such as the Southern Alps of New Zealand and the Central Range of Taiwan [*Wellman*, 1979; *Adams*, 1985; *Koons*, 1990; *Willett et al.*, 1993; *Willett*, 1999; *Willett et al.*, 2003] to large orogenic plateaus and their margins [*Willett et al.*, 1993; *Bilham et al.*, 1997; *Beaumont et al.*, 2001; *Hodges et al.*, 2001; *Beaumont et al.*, 2004] have lateral bedrock velocity components equal to or greater than the vertical components [*Willett et al.*, 2001].

[4] A characteristic shared by many active convergent mountain ranges, whether small or large, is an asymmetrical topographic profile in the cross-strike direction. Such asymmetry arises in small ranges formed over individual structures, such as fault-bend folds and fault-propagation folds. For example, the Siwalik Hills in the Himalayan foreland

[1]Department of Geosciences, Pennsylvania State University, University Park, Pennsylvania, USA.

0148-0227/07/2007JF000772$09.00

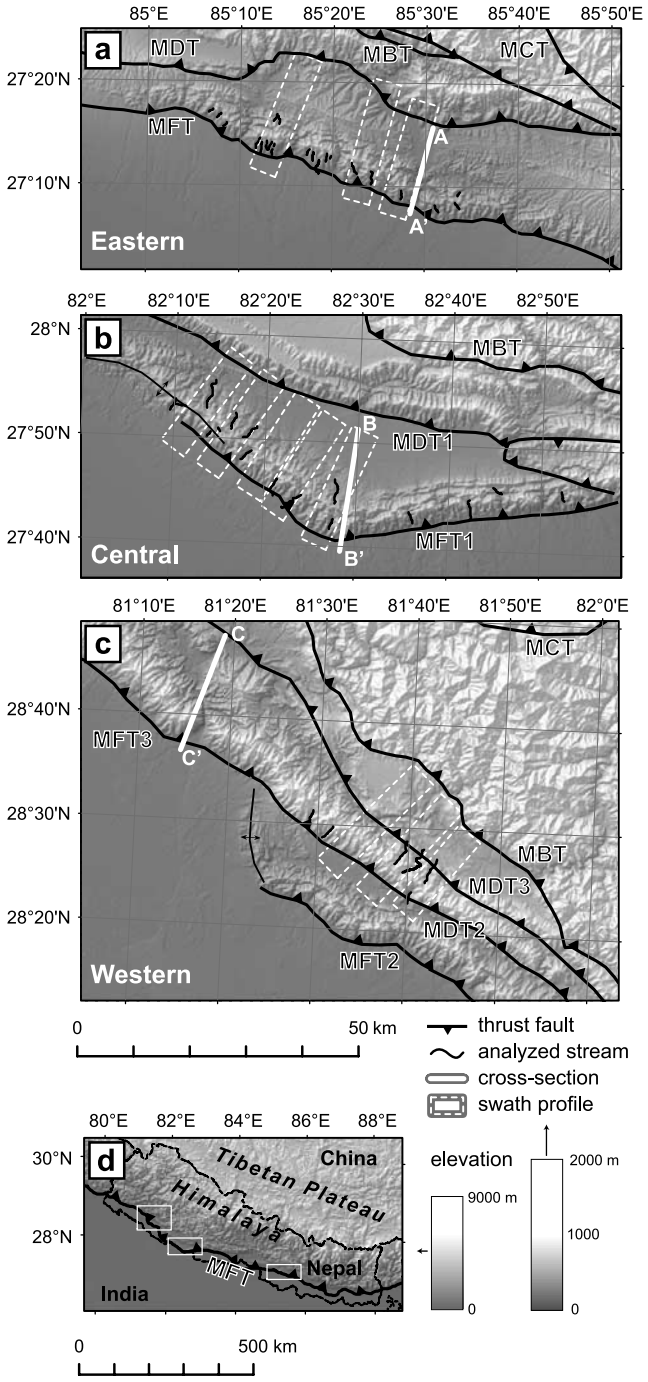

Figure 1. (a–c) Shaded relief maps of Siwalik Hills. Also shown are streams used in slope-area analyses, locations of swath profiles, and geologic cross sections (Figure 2). (d) Locations of regions in Figures 1a–1c, shown by white boxes. MFT, Main Frontal thrust; MDT, Main Dun thrust; MBT, Main Boundary thrust. Geology is after *Mugnier et al.* [1999] and *Lavé and Avouac* [2000].

(Figure 1) exhibit asymmetric profiles that are steeper in the direction of tectonic vergence (Figure 2) while maintaining a topographic steady state [*Hurtrez et al.*, 1999; *Lavé and Avouac*, 2000]. In some cases, small mountain ranges may exhibit asymmetry if base levels (e.g., basin elevations) on opposite sides of the range are unequal [*Ellis and Densmore*, 2006], although that is generally not the case in the Siwalik Hills. Moreover, entire orogens commonly have similar asymmetrical profiles. Examples include the Southern Alps of New Zealand, the Central Range of Taiwan, the Olympic Mountains of Washington State, and the Indo-Burman Range [see *Adams*, 1980; *Willett et al.*, 2001; *Whipple and Meade*, 2004]. These orogens have drawn the most attention. If such an orogen is at steady state, as these examples are thought to be, its topography appears to be an exception to *Gilbert*'s [1877] Law of Equal Declivities for equilibrium slopes as first pointed out by *Adams* [1985] in the Southern Alps. Recent explanations for these orogens' asymmetrical topography have incorporated reasonable climatic and tectonic boundary conditions. Various studies have attributed this asymmetry to the existence of resistant lithologic units serving as a cuesta-forming caprock [*Adams*, 1980, 1985], orographic precipitation creating spatially variable erosion rates [*Koons*, 1990; *Beaumont et al.*, 1992; *Batt and Braun*, 1999; *Willett*, 1999], and the mechanics of a doubly vergent critical wedge [*Koons*, 1990; *Willett et al.*, 1993; *Batt and Braun*, 1999; *Carena et al.*, 2002; *Whipple and Meade*, 2004].

[5] Recent modeling studies, however, provide a perhaps simpler explanation that steady state asymmetry in active orogenic settings can result from erosion in equilibrium with lateral bedrock motion [*Willett*, 1999; *Willett et al.*, 2001; *Herman and Braun*, 2006]. Topography develops toward a dynamically steady state such that over moderate timescales erosion balances lateral as well as vertical bedrock motions. How this balance occurs, and what its topographic signature might be, remain poorly understood. Three predicted outcomes of lateral motion have been put forth with respect to convergent orogens, particularly doubly vergent wedges [*Koons*, 1990; *Willett*, 1999; *Willett et al.*, 2001; *Herman and Braun*, 2006; *Stolar et al.*, 2006], but may be applicable to fault-bend folds as well. In doubly vergent wedges, bedrock streamlines may pass from the prowedge side through to the retrowedge side. First, lateral motion requires that erosion rates are greater on the retrowedge than the prowedge. Second, lateral motion is responsible for asymmetric steady state cross-sectional profiles of mountain ranges where the retrowedge surface is commonly steeper and narrower than the prowedge surface. Third, topography may be advected with bedrock. Drainage divides, for example, are transported to the point at which erosion on the retrowedge is rapid enough to halt further divide motion in a geographic reference frame.

[6] Although we have an improved understanding of the large-scale geomorphology that may result from lateral motion in convergent orogens, outstanding questions remain. First, we do not know whether the steady state position of the principal drainage divide, which is continually migrating in a bedrock reference frame, is controlled by hillslope diffusion [*Willett et al.*, 2001], stream incision [*Herman and Braun*, 2006], or other processes such as debris flow incision. Second, we still do not know the form of longitudinal profiles that will arise for a stream experiencing lateral bedrock motion. Because so many tectonic geomorphologic analyses today include stream profile analysis [e.g., *Lague et al.*, 2000; *Snyder et al.*, 2000; *Kirby and Whipple*, 2001; *Lavé and Avouac*, 2001; *Wobus et al.*, 2003;

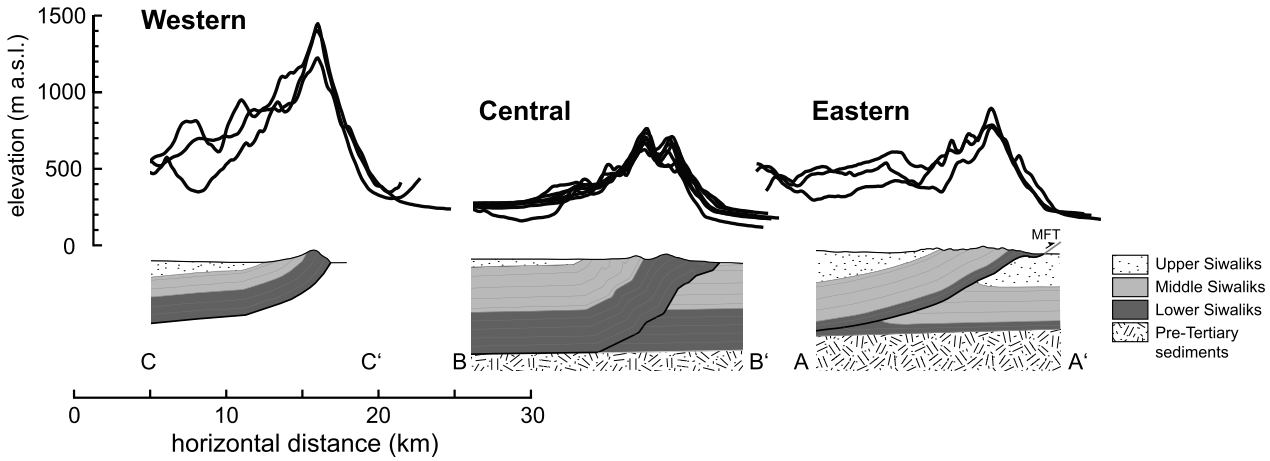

Figure 2. (top) Topographic profiles and (bottom) cross sections of the Siwalik Hills at 3 sites in Nepal (see Figure 1 for locations). Profiles are mean elevations along swaths 5 km wide. Cross sections for Siwalik Hills shown at bottom [after *Mugnier et al.*, 1999; *Lavé and Avouac*, 2000]. Vertical exaggeration of topographic profiles is 10×. Cross section is not vertically exaggerated. The western cross section is the closest to the western topographic profiles, but hanging wall thicknesses and fault geometries may be expected to differ between sites.

Hodges et al., 2004; *Wobus et al.*, 2006a] or applications of its methods to colluvial valleys [*Lague and Davy*, 2003], meaningful interpretations of bedrock deformation rates and styles require a theoretical understanding of the expected longitudinal profile forms and their sensitivities to lateral motion. In addition, field evidence for lateral advection is generally lacking because there is no theory regarding specific field-scale geomorphic manifestations of lateral motion that may provide testable predictions. In short, does lateral bedrock motion leave a unique fingerprint on the steady state landscape that can either be exploited or must be corrected for in tectonic geomorphic studies?

2. Approach and Scope

[7] Although previous work on lateral advection and landscape evolution in convergent orogens have used medium-sized orogens, specifically those thought to be doubly vergent wedges, as prototypes, such orogens are not ideal sites for testing the sensitivity of the landscape to lateral bedrock motion for a number of reasons. First, a strict comparison between model results and natural examples is hampered by orographic precipitation [*Anders et al.*, 2006; *Barros et al.*, 2006], complex geology comprising different lithologies, and commonly poorly constrained or complex bedrock kinematics [e.g., *McClay*, 2004]. Secondly, the large-scale asymmetry of such mountain ranges may arise from critical wedge mechanics in which the large-scale geometry of the mountain range is completely insensitive to erosion processes but rather is controlled by the geometry of underlying faults and internal frictional properties [*Koons*, 1990; *Carena et al.*, 2002; *Whipple and Meade*, 2004]. Thirdly, larger orogens such as the Southern Alps of New Zealand and the Olympic Mountains are shaped in part by glacial erosion [*Montgomery*, 2002; *Herman and Braun*, 2006].

[8] The present study avoids these complications by focusing on the effect of lateral bedrock motion on steady state fluvial topography of a mountain range bounded by a single structure with little or no internal deformation. We focus on relatively simple fault-bend folds, such as those that underlie many segments of the Siwalik Hills. At a number of sites in the Siwalik Hills, the long-term rock deformation rates are well constrained and deformation is described adequately by kinematic rules for fault-bend folding [*Lavé and Avouac*, 2000; *Mugnier et al.*, 2004], assuring us that comparisons with model results are justifiable.

[9] Our simulations and analyses focus thus on the adjustment of the fluvial system, particularly steady state longitudinal profiles, to lateral advection. Our work contrasts with previous landscape evolution models that investigated the topographic response to internal horizontal shortening and that fixed mountain range widths [*Willett et al.*, 2001; *Herman and Braun*, 2006]. Previous landscape evolution models on fault-bend folds, meanwhile, focused on sedimentation rather than geomorphology, were one-dimensional, and included diffusion as the only erosion rule [*Leturmy et al.*, 1995] or focused on the development of transverse drainage and the drainage patterns arising from lateral fault propagation and fault geometry [*Champel et al.*, 2002]. Other models have focused on the pre-steady-state topography developed above blind thrust faults [*Ellis and Densmore*, 2006].

[10] Our study is largely motivated by observations of topography and stream profile form in the Siwalik Hills. As such, our study begins with a quantitative characterization of the geomorphology of some of these ranges, focused particularly on their topographic asymmetry and the shapes of its bedrock stream profiles. Next, we establish predictions for steady state geomorphology in the presence of a uniform deformation field. Thus in section 4 we derive an expression for erosional flux on a steady state topographic surface, showing the expected nonuniformity of this quantity in the landscape. This section provides the fundamental ratio-

nale for expecting similar variability and asymmetry in topography. Topographic adjustment is demonstrated first in section 5, in which we derive a one-dimensional analytical solution for steady state detachment-limited stream slopes. This model provides simple, testable predictions of steady state stream profile shapes that are uniquely diagnostic of lateral bedrock motion, thereby providing a basis for understanding how one must account for such motion in stream profile analysis and in what cases such accounting is necessary. In order to incorporate realistic boundary conditions and multiple erosion processes, we present in section 6 the results of a numerical two-dimensional model of landscape evolution above a fault-bend fold above a planar ramp. This model simulates erosion by both detachment-limited stream incision and linear diffusion of hillslopes. Although fault ramps in nature may have some curvature, this analysis highlights the geomorphology that arises owing to a simple fault geometry and velocity field.

[11] The models presented here are limited because they include no feedbacks among surface processes, climate, and tectonics. For this reason the results may not be strictly applicable to orogens with complex deformation and climate patterns. However, for small structures and large orogens alike, we suggest that our approach has the advantage of isolating geomorphic responses to simple, though not unrealistic, tectonic boundary conditions and therefore outlines robust principles.

3. Siwalik Hills, Nepal: An Example of Asymmetrical Steady State Topography

3.1. Background

[12] The Siwalik Hills of Nepal are a series of linear ridges ~15 km in width and up to ~1300 m in total relief. The region has a humid and hot monsoonal climate and receives over 2000 mm of precipitation annually [*Hurtrez et al.*, 1999]. These ridges have formed over active fault-bend and fault-propagation folds on the Main Frontal Thrust (MFT) and Main Dun Thrust (MDT) and are thus the southernmost topographic expressions of active deformation within the Himalayan orogen (Figure 1). Hanging wall deformation of Miocene to Pleistocene fluviatile siltstones, sandstones, and conglomerates of the Lower, Middle, and Upper Siwalik Group and negligible changes in bed thickness are consistent with flexural slip and kink-band migration predicted by kinematic models of fault-bend folds [*Lavé and Avouac*, 2000; *Mugnier et al.*, 2004]. Differences in erodibility, both to fluvial incision and hillslope diffusion, between the Lower and Middle Siwalik units, which underlie our study areas, are negligible [*Hurtrez et al.*, 1999; *Mugnier et al.*, 1999; *Lavé and Avouac*, 2001]. Nevertheless, erodibility is high: up to 2 orders of magnitude greater than in the Lesser and Higher Himalaya [*Attal and Lavé*, 2006]. Combined fault slip rates between the MFT and MDT over the Quaternary are 0.19–0.21 mm/a [*Lavé and Avouac*, 2000; *Mugnier et al.*, 2004]. Furthermore, Quaternary erosional fluxes over sections of fault-bend folding have approximately equaled tectonic fluxes, indicating the achievement of flux and approximate topographic steady states that make these sites appropriate for comparison to model results [*Hurtrez et al.*, 1999; *Lavé and Avouac*, 2000].

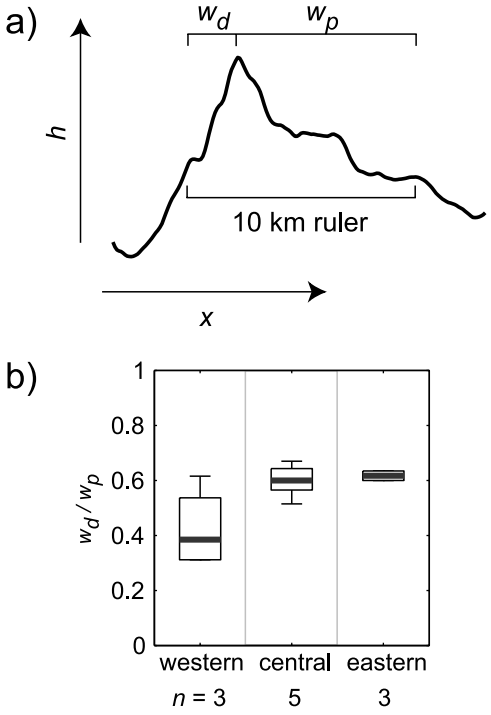

Figure 3. (a) Example profile from the western Siwalik Hills site, with 10× vertical exaggeration, showing measurements of distal and proximal ridge flank widths (w_d and w_p, respectively) of a set ruler length (10 km). (b) Boxplot of ridge-flank width ratios, w_d/w_p, based on minimum elevation swath profiles from the western, central, and eastern Siwalik Hills. Boxplot shows median, quartile range, and total range. Profile locations are shown in Figure 1.

3.2. Topography

[13] Topography was characterized for three segments of the Siwalik Hills in eastern, central, and western Nepal using metrics for the asymmetry of cross-range topographic profiles and the concavity and steepness of stream profiles. All analyses were conducted in a geographic information system environment using 3 arc-second (~90 m) resolution Shuttle Radar Topographic Mission (SRTM) digital elevation models (DEMs).

[14] The asymmetry of the Siwalik Hills, demonstrated above (Figure 2), can be quantified by a ridge-flank width ratio, w_d/w_p: the ratio of the distal flank's width divided by the proximal flank's width. Because actual flank width may be a function of base level [*Ellis and Densmore*, 2006], we simplify analysis of the Siwalik Hills by defining boundaries at a common elevation and spaced with a ruler of fixed length, in this case 10 km (Figure 3a). Thus this metric is essentially a ratio of flank slopes. The ridge-flank width ratio of the Siwalik Hills, measured from profiles representing the minimum elevations in 5-km-wide swaths, incorporating stream profiles, has a mean value of 0.54 ± 0.08 at the 95% confidence level for 11 profiles among 3 segments of the range, indicating that the distal flank is generally about half the width of the proximal flank.

[15] This asymmetry can be explained effectively as the result of contrasting stream profile shapes on the distal and

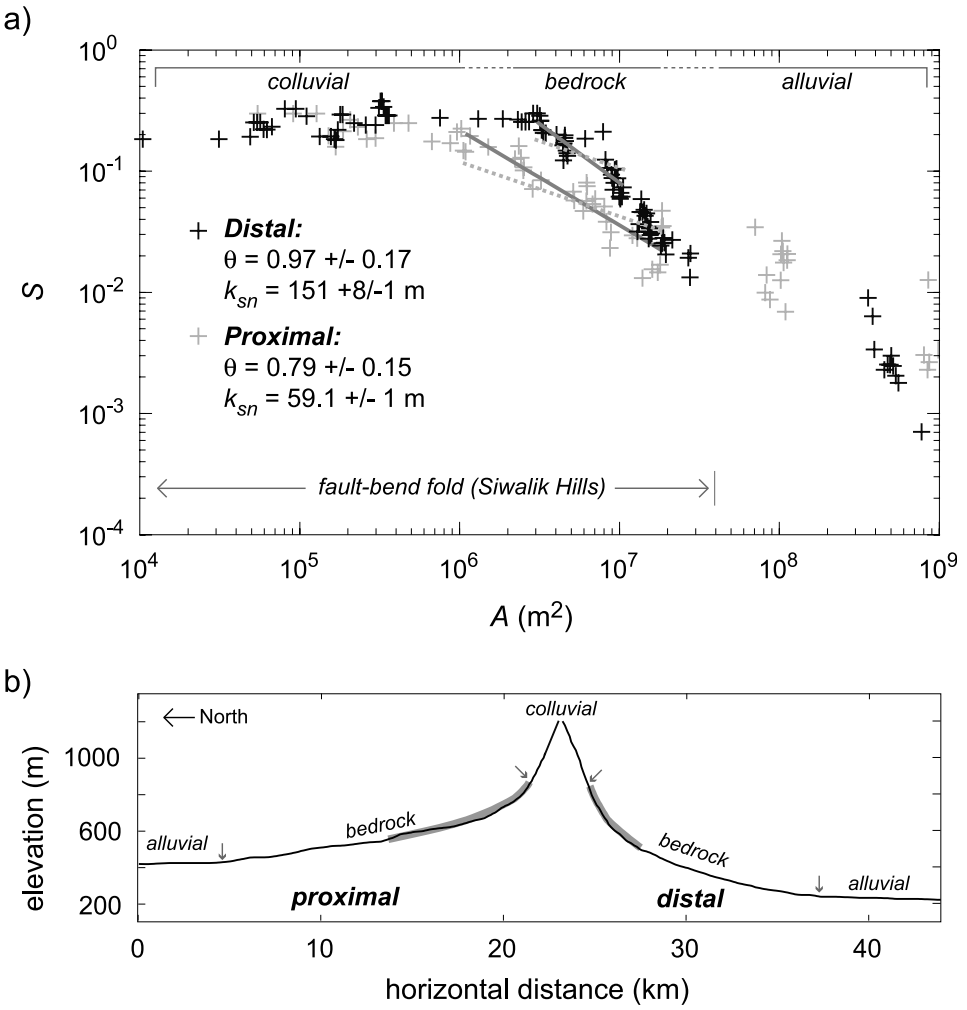

Figure 4. (a) Representative slope-area plots of streams that flow perpendicular to strike in the western Siwalik Hills for the proximal or north-facing side of the ridge and the distal or south-facing side of the ridge. Both θ and k_{sn} are shown for the individual bedrock fluvial channels shown. Solid lines represent regressions used to determine θ; dashed lines show regressions with θ_{ref} = 0.5. Stream slopes and drainage areas were extracted from a 90-m SRTM DEM. (b) Longitudinal profiles of the streams in Figure 4a. Geomorphologic process regions (colluvial, bedrock stream, and alluvial stream) shown were interpreted from scaling relations in Figure 4a. Vertical exaggeration is 10×.

proximal ridge flanks. Bedrock stream profile shapes are commonly quantified using parameters describing their commonly empirically observed inverse power law relation between drainage area (A) and channel slope (S),

$$S = k_s A^{-\theta}, \tag{1}$$

where k_s is termed the steepness index, with units of $m^{2\theta}$, and θ is the concavity index [*Snyder et al.*, 2000; *Kirby and Whipple*, 2001; *Wobus et al.*, 2006a]. Concavity index is commonly 0.4–0.7, in general agreement with theoretical considerations [see *Whipple*, 2004, and references therein]. In steady state stream profiles, this range has been attributed to factors such as streamwise variations in sediment delivery and size [*Sklar and Dietrich*, 1998], rock uplift rate [*Kirby and Whipple*, 2001], lithology [*Moglen and Bras*, 1995], or orographic precipitation [*Roe et al.*, 2002]. Steepness index is expected to vary as a function of uplift rate and erosivity (combining lithology, river width, climate) [*Snyder et al.*, 2000]. For purposes of comparison among streams, a normalized steepness index, k_{sn}, is often calculated using a reference concavity index, θ_{ref} [see *Wobus et al.*, 2006a]. When θ_{ref} = 0.45, k_{sn} is commonly between 20 and 600 $m^{0.9}$ [*Whipple*, 2004].

[16] Stream profiles extracted from the DEMs of the Siwalik Hills in the manner described by *Wobus et al.* [2006a] exhibit inverse power law scaling between slope and drainage area in the region of bedrock streams over a range of A between 10^6 and 10^8 m^2 and where streams lie above the fault-bend fold (Figure 4). At smaller drainage areas, channels are usually colluvial/debris flow [*Lague and Davy*, 2003]. At larger areas, channels exit the fold and are alluvial [*Kirby and Whipple*, 2001]. Concavity indices range from 0.6–1.2 on the proximal side and 0.5–2.1 on the distal side. Similar values >0.5 were reported by *Kirby and Whipple* [2001]. The normalized steepness index was cal-

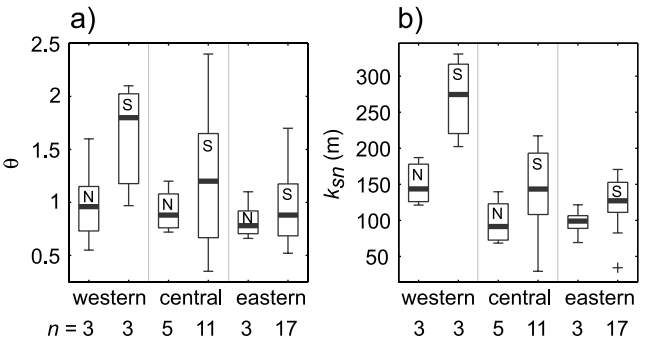

Figure 5. Boxplots of (a) θ and (b) k_{sn} for different regions of the Siwalik Hills, measured from 90-m-resolution SRTM DEMs. Values shown for proximal north-flowing, N, and distal south-flowing, S, streams. Sample sizes, n, are shown at bottom.

culated by fitting a regression with a reference concavity of 0.5, which is similar to the value of 0.46 used by *Kirby and Whipple* [2001] and allows comparison with model results in later sections where $\theta_{ref} = 0.5$. (We note that the k_{sn} is strictly meaningful only when the difference between θ and θ_{ref} is <~0.2 [*Wobus et al.*, 2006a], but argue that our choice simplifies comparison with model results.) Normalized steepness indices range from 68–186 m and 29–330 m on the distal side. It is evident that distal streams at each site have both greater median normalized steepness indices and concavity indices than observed proximal streams (Figure 5). We also note that k_{sn} and θ generally increase from east to west and that the difference in each parameter between proximal and distal ridge sides also increases from east to west. Also, the ratio of steepness varies systematically with the ridge-flank width ratio, supporting a basic link between stream profile shape and range asymmetry. Thus the narrower, distal ridge flanks correspond with steeper, more concave streams and vice versa. However, such variations in stream steepness and concavity require explanation. In the following sections we explore the possible role of lateral advection.

4. Rock Flux Through Steady State Topography

[17] Particle pathways through orogens have been known to be nonvertical and thus affect our interpretation of erosion rates. This has been noted in thermochronologic studies that infer long-term erosion or exhumation rates from mineral cooling rates [*Morris et al.*, 1998; *Walcott*, 1998; *Batt and Brandon*, 2002; *Willett et al.*, 2003; *Bollinger et al.*, 2004]. As an illustration, it is estimated that simple predictions of steady state sediment yield in the western flank of the New Zealand Southern Alps that account for only the vertical component of tectonic motion underestimate measured yields by 600% [*Walcott*, 1998]. In a similar fashion, inclined bedrock pathways near Earth's surface may impact short-term erosion rate estimates, such as those based on fluvial terrace records [*Pazzaglia and Brandon*, 2001; *Tomkin et al.*, 2003]. Such calculations have often been made for streams with gentle slopes, where erosion rates have probably only been underestimated by <5% [e.g., *Lavé and Avouac*, 2000; *Kirby and Whipple*, 2001]. The role of lateral advection on erosion rates, and why these rates are a function of slope, can be simply visualized and quantified.

[18] On the basis of a simple graphical exercise, we expect erosion rates to vary as a function of aspect, slope, and inclination of bedrock streamlines, as can be envisioned for a basic two-sided mountain range (Figure 6). We will refer to the two sides of the mountain range as proximal and distal, reflecting their relative positions near and far, respectively, from the source of advected hanging wall bedrock. These sides are analogous to the prowedge and retrowedge, respectively, of the doubly vergent wedge. For a given bedrock velocity, V, crossing a cell of unit horizontal width, dx, topographic slopes facing in the direction of lateral advection, such as those on the distal side, will experience greater steady state erosional fluxes than proximal slopes. Similarly, the concave profiles common among streams also imply that spatial variations in steady state erosional fluxes will occur along a single stream.

[19] A generic one-dimensional solution for the above flux of rock through a steady state topographic surface can be derived. As a first step, the change in topographic elevation with time is given by the continuity equation

$$\frac{\partial h}{\partial t} = u - v\frac{\partial h}{\partial x} - h\frac{\partial v}{\partial x} - E, \tag{2}$$

where h is topographic elevation (m), t is time (annums), u and v are the vertical and horizontal components, respectively, of bedrock velocity V (m · a^{-1}), and E is erosion rate (m · a^{-1}). Note that this notation goes against the convention in physics where u is the x-directed velocity but conforms with common geologic usage where u is rock uplift rate.

[20] At steady state and where rock velocity is vertical, the unit tectonic flux of rock passing through a steady state

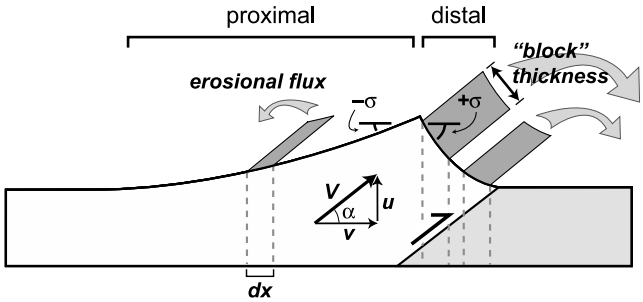

Figure 6. Cross section of a generic mountain range bounded by a single thrust fault and with no internal strain, showing the combined effect of topographic slope angle parallel to the direction of advection, σ, and rock particle trajectory angle or fault dip, α, on erosional flux predicted from a horizontal unit cell at steady state. Erosional flux for an arbitrary unit of time is depicted by gray blocks extruding from the surface, the thicknesses of which are functions of σ, α, and dx. Bedrock has velocity V with vertical and horizontal components u and v, respectively. Note that lateral advection and nonhorizontal topography create spatial variations in erosion rate, both between oppositely oriented ridge flanks and along a single, curved stream profile.

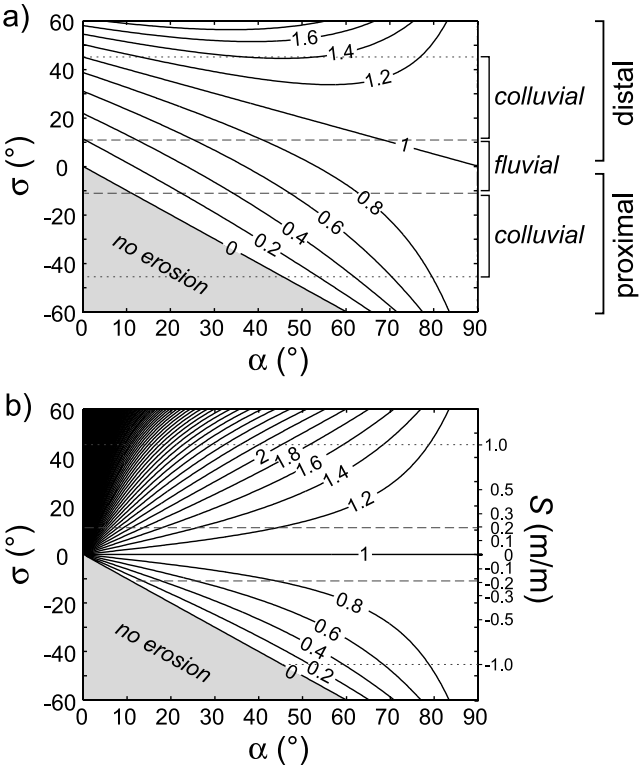

Figure 7. Nomograms showing how erosion rate varies as a function of topographic slope angle, σ, and bedrock streamline inclination angle, or ramp dip, α. Slope and horizontal bedrock motion are in the x direction. Positive slopes face in the direction of lateral bedrock motion. (a) Contours representing nondimensional erosion rate, E^*, where $E^* = E/V$. (b) Contours representing the ratio of the erosion rate to its vertical component. Regions of a steady state landscape with greater erosional fluxes than rock uplift rates plot in the top halves of both graphs. The suggested domains of fluvial channels and colluvial channels are marked with dashed lines [*Sklar and Dietrich*, 1998; *Lague and Davy*, 2003; *Stock and Dietrich*, 2003], although this transition is approximated and the exact process or suite of processes occurring at steep slopes is poorly understood. Regions where steady state erosion is not possible marked in gray. Contour interval is 0.2. Slope values, S, that correspond to the topographic slope angles are shown on the secondary axis in Figure 7b.

land surface of horizontal dimensions dx and dy will equal the erosion rate at steady state, or more specifically the unit erosional flux, E, such that $E = u$. In this case, the flux of material through a unit cell of the land surface is only a function of rock uplift rate. However, where rock velocity is not vertical, topographic slope becomes an important variable and may impart nonuniform steady state erosional fluxes (Figure 6). Steady state unit erosional flux is written

$$E = V \cdot \sin(\alpha + \sigma)/\cos\sigma, \tag{3}$$

where α is the inclination angle (°) of the bedrock streamline in the x direction and σ is the angle of topographic slope in the x direction (°), or $\sigma = \text{atan}(-dh/dx)$. Solutions to (2) show that the rate of erosion varies as a function of the slope of the land surface and the inclination of bedrock particle paths (Figure 7). This variability is largest on steep slopes. In the region of bedrock streams, which commonly have slopes up to ~0.2, or ~11° [*Seidl and Dietrich*, 1992; *Lague and Davy*, 2003], the erosional flux of material through a streambed of unit dimensions can be 130% the vertical component (for a reasonable $\alpha = 30°$). Steeper streams exist and may approach slopes of 1 [e.g., *Schoenbohm et al.*, 2004; *Wobus et al.*, 2006b] highlighting the facts that the dominant erosion mechanism in steep channels is poorly understood but remains an area of active research [e.g., *Stock and Dietrich*, 2003; *Crosby et al.*, 2007] and the fluvial-colluvial transition is probably much broader than any singular transition slope value implies. In the field of debris flow channels and hillslopes, with gradients up to ~1, or ~45° [*Lague and Davy*, 2003; *Stock and Dietrich*, 2003], the total flux can be 270% the vertical component. The difference in steady state erosional fluxes between proximal and distal fluvial channels, therefore, could commonly be as much as 60%; for debris-flow channels, this difference could be as much as 340%. Because erosion rate is typically modeled as a function of topographic slope and contributing drainage area [e.g., *Dietrich et al.*, 2003], we expect that spatial variations in erosion rates imposed by nonvertical rock velocities should generate a distinctive landscape form.

5. Analytical Stream Profile Model

5.1. Derivation

[21] Because bedrock stream channels form the lower boundary conditions for hillslopes in most mountain ranges, a basic approach to understanding the role of lateral advection requires as a first step an understanding of fluvial geomorphology in such a setting. An analytical solution for stream slopes that accounts for a horizontal component of bedrock velocity on distal and proximal ridge flanks, as depicted in Figure 6, is derived below and allows us to predict stream profile shapes.

[22] We start with the postulates that fluvial erosion of bedrock channels is detachment-limited and that the erosion rate is proportional to unit stream power [*Howard et al.*, 1994]. Although it does not explicitly account for the possible role of sediment in bedrock abrasion [*Sklar and Dietrich*, 1998, 2001; *Whipple and Tucker*, 2002; *Sklar and Dietrich*, 2004], the unit stream power equation has been found to satisfactorily predict erosion rates in a number of tectonically active settings [*Stock and Montgomery*, 1999; *Snyder et al.*, 2000; *Kirby and Whipple*, 2001]. Following existing derivations [e.g., *Whipple and Tucker*, 1999], we assume common scaling relations for basin hydrology and channel hydraulic geometry, that all discharge derives from overland flow, that precipitation is spatially and temporally constant, and no infiltration or evapotranspiration. In the case where there is no lateral advection ($v = 0$), elevation change with time is given by the continuity equation

$$\frac{\partial h}{\partial t} = u - KA^m S^n, \tag{4}$$

where K is a coefficient of erodibility with units of $\text{m}^{(1-2\text{m})}\text{a}^{-1}$ and m and n are exponents. The rightmost term

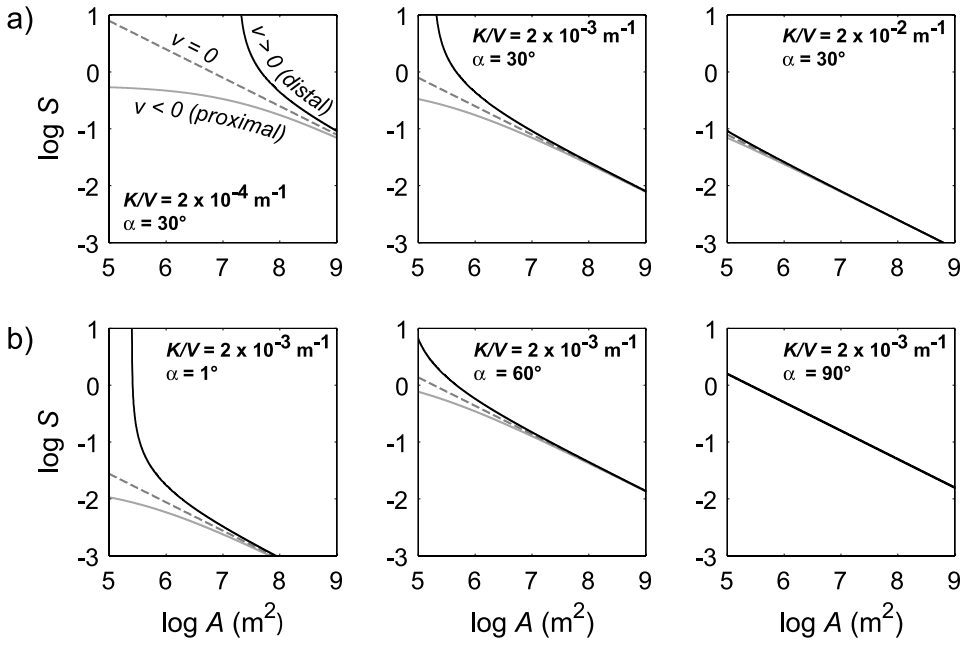

Figure 8. Plots showing the analytical solutions of stream gradient as a function of drainage area for (a) different values of K/V and (b) different values of α. Results are plotted for streams that flow in the direction of bedrock motion ($v > 0$), perpendicular to this direction ($v = 0$), and against the direction of bedrock motion ($v < 0$).

is the erosion rate; for erosion rate proportional to unit stream power, $m = 0.5$ and $n = 1$ [*Whipple and Tucker*, 1999], and these exponents are used throughout this study. Solving (4) for steady state stream gradient yields

$$S = \left(\frac{u}{K}\right)^{1/n} A^{-m/n}. \tag{5}$$

The similarity in form between (5) and (1) has been the basis for numerous studies aimed at determining the values of m and n, erodibility, K, and rock uplift rate, u, from empirical data [e.g., *Snyder et al.*, 2000; *Kirby and Whipple*, 2001; *Duvall et al.*, 2004].

[23] If lateral bedrock motion is nonzero and spatially constant (i.e., no internal horizontal shortening), elevation change with time is given by

$$\frac{\partial h}{\partial t} = u - v\frac{\partial h}{\partial x} - KA^m S^n. \tag{6}$$

At steady state, (6) can be rewritten as

$$v\frac{\partial h}{\partial x} + KA^m\left(-\frac{\partial h}{\partial x}\right)^n = u, \tag{7}$$

where $S = -dh/dx$. A general solution for $h(x, t)$ with variable n does not exist, so we derive a solution for the case of $n = 1$. The steady state one-dimensional solution of stream gradient is thus

$$S = \frac{u}{KA^m - v}. \tag{8}$$

For analysis, we nondimensionalize (8) with the following relations:

$$\cos\alpha = v^* = v/V \tag{9}$$

$$\sin\alpha = u^* = u/V, \tag{10}$$

such that

$$S = \frac{\sin\alpha}{\frac{KA^m}{V} - \cos\alpha}, \tag{11}$$

where K/V represents an efficacy of fluvial erosion processes relative to bedrock velocity.

[24] The solutions that follow are distinguished by streamflow direction and by the bedrock deformation field. We consider streams that flow in the direction of advection ($v > 0$), as would occur on the distal side of a mountain range, streams that flow against the direction of advection ($v < 0$), as on the proximal side of the range, and streams experiencing no lateral advection ($v = 0$). First, we predict stream profiles that develop over a uniform bedrock velocity field, such as would occur over a planar ramp, and then profiles that develop constant lateral gradients in u and v exist, such as over a curved ramp with uniform curvature. Bedrock erodibility is assumed uniform.

5.2. Results

5.2.1. Stream Profiles Above a Straight Ramp

[25] For nonzero v and when the ratio K/V is sufficiently low, the slope-area relation predicted by (11) is generally curved in log-log space: concave for distal streams and convex for proximal streams (Figure 8). This contrasts with

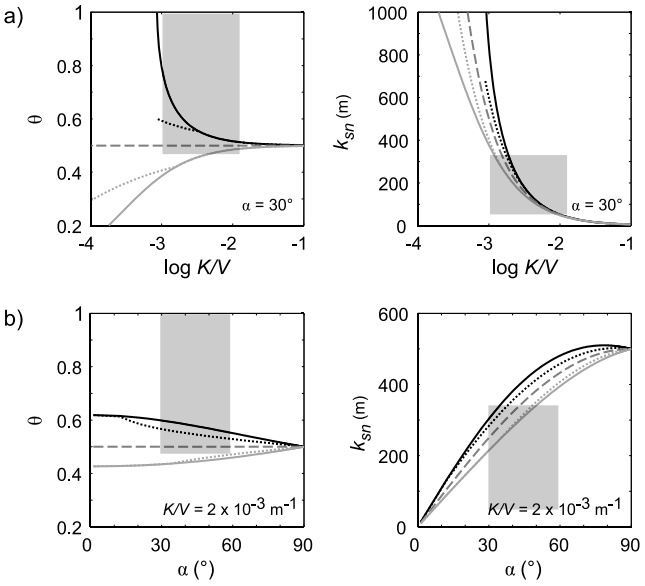

Figure 9. Plots showing how concavity index, θ, and normalized steepness index, k_{sn}, vary as a function of (a) K/V and (b) α for streamflow relative to direction of bedrock motion. Symbology is the same as in Figure 8. Dotted lines indicate results of regressions only for those data with $S < 0.2$, which may be more representative for most streams. Here θ and k_{sn} are calculated using least squares linear regression over the range $A = 10^6$ m^2 to 10^8 m^2. Normalized steepness index was calculated using $\theta_{ref} = 0.5$. Gray boxes show approximate parameters of the Siwalik Hills.

the power law relation for streams that experience pure rock uplift ($v = 0$). This disparity increases as K/V and/or α decrease. The differences among slope-area relations are most pronounced at small drainage areas where slopes are steepest and the effect of lateral advection on erosion rate is therefore greatest. It should be noted that these plots also extend to slope-area space that may be unrealistic for bedrock streams and therefore they must be interpreted with caution.

[26] On the proximal ridge flank at small drainage areas, stream slopes approach a limiting value, S_{max}, where $S_{max} = -\tan \alpha$. This reflects the fact that steady state topographic slopes cannot exceed the inclination of bedrock streamlines. Therefore at their steepest, steady state slopes might parallel bedding (if bedding is parallel to the underlying fault) and give the false impression that resistant beds control the local geomorphology. As a corollary, slopes that are steeper than α must be transient.

[27] In contrast, stream gradients on the distal flank become infinite at low drainage areas. This limit occurs at a critical area, A_{min}, where $A_{min} = (v/K)^{1/m}$ and thus increases for smaller α and/or K/V. In reality, these slopes will steepen to the point of mass failure or enter a different process zone (e.g., debris flows) more readily than slopes facing the opposite direction or experiencing pure rock uplift.

[28] Steepness and concavity indices can be estimated for these cases by fitting a linear regression equation to data over a specified range. Although our model predicts the slope-area relation may be curved in log-log space and therefore not always accurately described by a power law, we fit a power law for consistency with the existing literature and to allow a simple comparison among model results. Thus we fit a line to points along the model stream with drainage area, A, between 10^6 and 10^8 m^2 using a $\theta_{ref} = 0.5$. This range is consistent with that of bedrock streams in the Siwalik Hills [*Kirby and Whipple*, 2001; *Lague and*

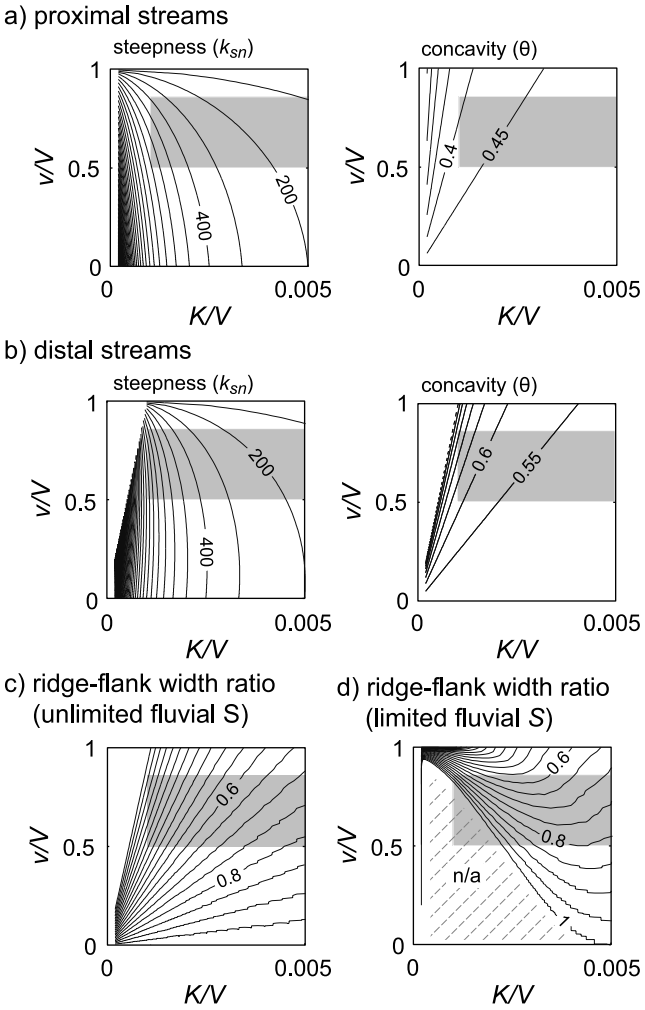

Figure 10. Contour plots of concavity (θ) and steepness index (k_{sn}) in parameter space of nondimensional lateral advection (v/V) and erosivity relative to bedrock velocity (K/V); θ and k_{sn} calculated over full range of A from 10^6 to 10^8 m^2 for (a) proximal streams and (b) distal streams. (c) Ridge-flank width ratio (w_d/w_p) calculated using model stream profiles with no maximum slope. See text for details. (d) Ridge-flank width ratio calculated using a maximum stream slope, $S = 0.2$. All higher elevations are set to this same slope. Although hillslope lengths may not be accurate, it estimates a likely end-member width ratio for comparison to Figure 10c. Note that asymmetry is not calculated at very low K/V because stream slopes <0.2 are not present. Steepness index plots have contour interval = 100 m; concavity plots have contour interval = 0.05; flank width ratio plots have contour interval = 0.05. Gray boxes show approximate parameter space of Siwalik Hills.

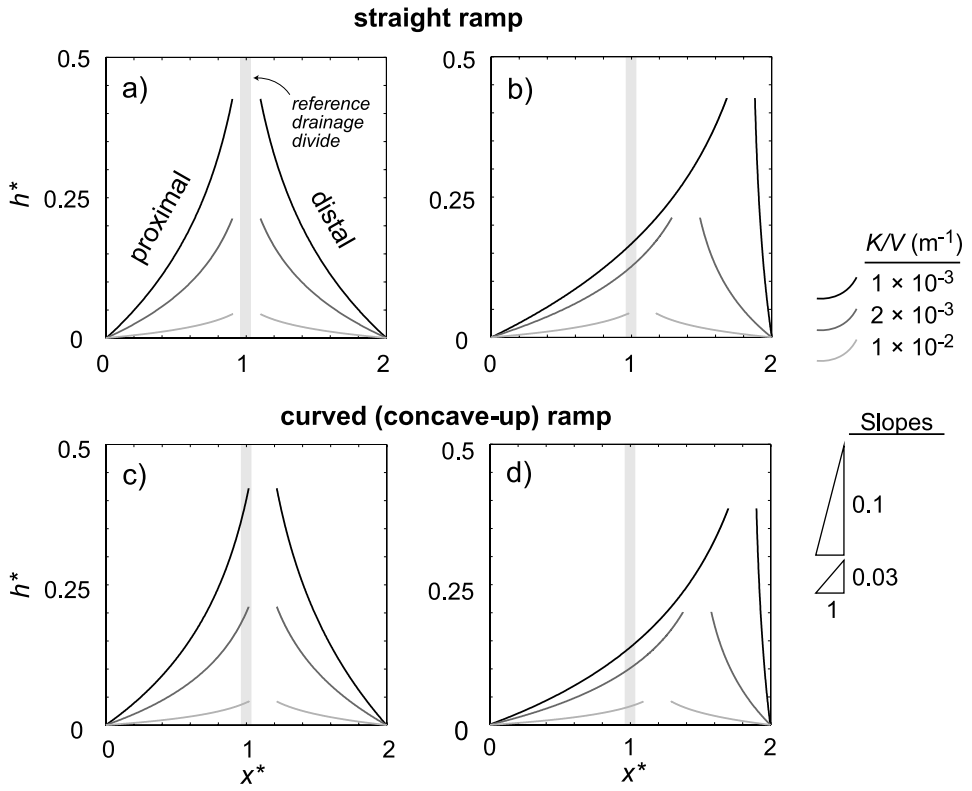

Figure 11. Longitudinal stream profiles for a two-sided, 1-D mountain range. Profiles were produced for bedrock velocity fields found above (a, b) straight and (c, d) curved fault ramps. Bedrock moves from left to right. In Figures 11a and 11c, the horizontal velocity term in (8) is ignored whereas it is included in Figures 11b and 11d. For the straight ramp, $\alpha = 30°$. For the curved ramp, mean $\alpha = 30°$ and $du/dx = 1.2 \times 10^{-6}\ m^{-1}$. Note that results for the curved ramp are sensitive to k_x and η. In the present example, $k_x = 0.1$ and $\eta = 0.5$. The channel head is defined where $A = 10^6\ m^2$ or $A = A_c$, whichever is greater. The nondimensional interchannel-head distance is defined arbitrarily as 0.2. Cumulative stream length and interchannel-head distance are fixed at 2.

Davy, 2003]. Reference concavity is chosen on the basis of model parameters m and n in (5). However, the calculated regression parameters depend on the regression range. Linear regressions can be fit to the curve over this entire range or to only that portion of the curve with slopes less than an arbitrary value (e.g., 0.2), representing a hypothetical slope-determined transition to channels formed by colluvial processes such as debris flows [e.g., *Stock and Dietrich*, 2003].

[29] Distal streams have greater concavity and steepness indices than proximal streams. This is clearly seen when we vary K/V or α alone (Figure 9). Fitted concavity and steepness differ most from the case where $v = 0$ when erodibility relative to velocity is small or ramp dip is gentle, which is more generally observed over a plot of ramp dip, expressed as v/V, versus K/V parameter space (Figure 10). These differences are negligible where K/V is large because steady state slopes are predicted to be gentle in such cases and variations in erosion rate owing to aspect are therefore small. The differences similarly decrease as v/V, and thus ramp dip, increases and erosion rate becomes more uniform. This variation with ramp dip demonstrates that whereas concavity index does not vary as a function of u [*Whipple and Tucker*, 1999], it does vary as a function of v.

[30] Plotting longitudinal stream profiles allows one to visualize the effect of varying these parameters on range asymmetry. By Hack's Law,

$$A = (x/k_x)^{1/\eta}, \tag{12}$$

where k_x is a coefficient, the exponent $\eta \approx 0.5$ [*Hack*, 1957], and x is the distance downstream from the channel head. Substituting (12) into (11) and setting the channel head to a drainage area of $10^6\ m^2$, we produce distal and proximal stream profiles using the forward Euler method (Figures 11a and 11b). In this reference frame, $v > 0$ for distal streams and $v < 0$ for proximal streams. The combined profiles are plotted over an arbitrary total length ($x^* = 2$), and thus stream profiles represent to first order the basic cross-sectional shape of a small mountain range with equal base-level elevations on both sides and where erosion is dominantly fluvial. Note that this shape is symmetrical when $v = 0$ and it is nearly symmetrical at large K/V when $v > 0$ (Figures 10c, 10d, 11a, and 11b). In contrast, the cross-sectional shape is increasingly asymmetrical at lower K/V.

5.2.2. Stream Profiles Above a Curved Ramp

[31] Next, we consider the effects on stream profile form imparted by nonuniform u and v, such as above a curved, concave-up ramp. Proximal and distal stream profiles are

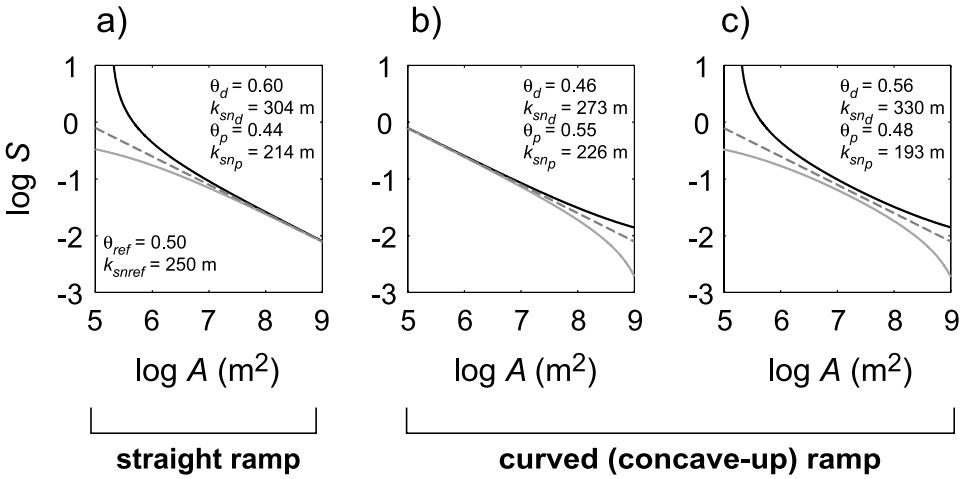

Figure 12. Slope-area plots comparing the effects of two ramp geometries (straight and curved) on steady state detachment-limited streams profiles. (a) Stream erosion balancing vertical and lateral rock motion above a straight ramp ($\alpha = 30°$). (b) Curved ramp, and erosion balancing rock uplift only. (c) Curved ramp, and erosion balancing lateral advection and rock uplift. The curved fault produces a uniform horizontal gradient in rock uplift rate ($du/dx = 1.2 \times 10^{-6}$ a^{-1}) with a mean $\alpha = 30°$, similar to that near the Bakeya River in the Siwalik Hills, Nepal [*Lavé and Avouac*, 2000]. $K/V = 2 \times 10^{-3}$ m^{-1} in all simulations. Line symbology is the same as for Figure 8. Though not shown in separate plots, the slope-area relationships for streams above straight ramps that balance only the vertical components of tectonic flux plot along the dashed reference lines. For all simulations, k_{sn} and θ calculated by regression between $A = 10^6$ and 10^8 m^2. For curved ramp simulations, $k_x = 0.1$ and $\eta = 0.5$.

calculated for a single ridge and uniform lateral gradients in u and v produced by a best fit concave fault ramp to that in the eastern Siwalik Hills site shown in Figure 1. In contrast to the one-dimensional streams generated over a straight ramp (Figure 12a), streams on a single ridge formed over a curved ramp and accounting only for vertical bedrock velocity show the largest differences in slope at large drainage areas (Figure 12b). This is because points with small drainage areas lie close to the range divide and thus experience similar rates of uplift, in contrast to downstream reaches. Accounting for both u and v produces slopes that diverge at small and large drainage areas (Figure 12c). The signature of lateral advection in stream profiles is therefore strongest (1) when comparing slope-area data of both distal and proximal streams, (2) when the stream heads are close and therefore likely experience similar rock uplift rates, and (3) where the gentler proximal and steeper distal slope-area trends converge in the downstream direction.

[32] Curved ramps impart asymmetry because of both a spatial gradient in u as well as the fact that $v > 0$. This is apparent if we calculate stream profiles accounting only for u and if we account for both u and v (Figures 11c and 11d). Importantly however, if one accounts only for u, profile asymmetry is only a function of ramp curvature and changes in K/V, due to changes in climate or fault slip rate, do not affect asymmetry. In contrast, models with lateral advection predict that changes in climate or bedrock velocity will produce changes in steady state asymmetry.

5.2.3. Comparison to the Siwalik Hills

[33] The Siwalik Hills lie in a region of parameter space where a topographic response to lateral advection is predicted (Figure 10). For example, the 1-D model predicts that in the expected parameter space, and for commonly occurring stream slopes ($S < 0.2$), k_{sn} may vary between proximal and distal streams by up to a factor of 2, with the distal streams being steeper, even though rock uplift rates are equal (Figure 9). Steepness indices in the Siwalik Hills are consistent with this (Figure 9). Ridge-flank width ratios measured in the Siwalik Hills, ranging from ~0.3 to 0.7, are consistent with simple 1-D model predictions (Figures 10c and 10d). Similarly, predicted concavity index may vary between proximal and distal streams by up to 0.2, with the distal streams being the more concave of the set. This is generally observed in the Siwalik Hills, although the median difference measured in the western site is considerably greater (~0.75).

[34] Concavity indices on both ridge flanks in the Siwalik Hills are, however, significantly larger than predicted by models. One possible explanation is that this is due to downstream decreases in rock uplift rate. Rock uplift rate gradients are known to exist at the easternmost of our three sites because the ramp is slightly curved [*Lavé and Avouac*, 2000] and the uplift rate gradients are thought to affect stream concavity here [*Kirby and Whipple*, 2001]. At this site, the axis of maximum rock uplift rate occurs a short distance south of the range crest and is associated with an inflection in the dip of the fault (Figure 2). The fact that θ is >0.5 in both proximal and distal streams has been previously documented and attributed to downstream decreases in rock uplift rate [*Kirby and Whipple*, 2001]. A similar inflection in the dip of the fault in the central Siwalik Hills site [*Mugnier et al.*, 1999] could affect concavity there in similar ways. However, at the western site strata dips decrease northward from the fault trace [*Mugnier et al.*,

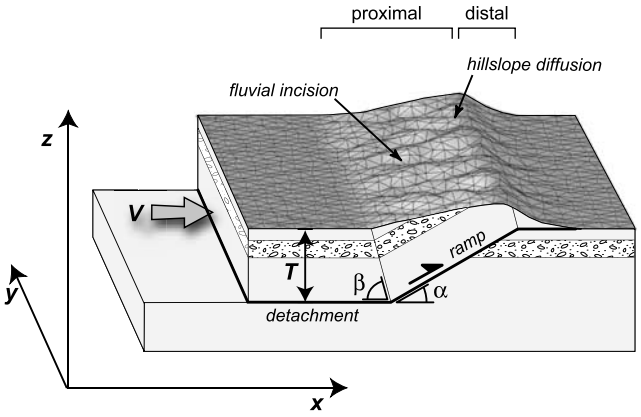

Figure 13. Schematic configuration of the fault-bend fold model used in the landscape evolution simulations, showing the model's computational mesh. Strata are shown only for visual purposes and do not reflect lithologic conditions in the simulations. Erosion has occurred in the case shown. The dips of the detachment and upper flat are 0°. Note that entire length of model ridge in y direction is not shown.

1999] and a downstream decrease in rock uplift rate is not expected under distal streams.

[35] A more compelling comparison is based on the form of slope-area plots. Although gradients in rock uplift rate are present in the Siwalik Hills and may thus affect concavity and steepness indices, slope-area plots of paired proximal and distal streams (Figure 4) that converge in the downstream direction owing to lateral advection. Whereas the model predicts deviations in the slope-area trend from power law form, these departures are most pronounced outside of the range of slopes and drainage areas associated with bedrock fluvial channels in the Siwalik Hills. Instead, these occur in areas more likely dominated by colluvial or alluvial processes. Thus the non-power-law behavior of the model probably does not negate our primary results.

[36] The analytical solutions for stream gradient and the resulting stream profiles demonstrate the importance of horizontal bedrock motion but neglect a range of other surface processes that may be present. Furthermore, these solutions are for only the simplest boundary conditions. With a numerical model, we can explore the effect of hillslope processes and the response of the landscape to the more realistic tectonic boundary conditions of a fault-bend fold.

6. Numerical Model of Landscape Evolution on a Fault-Bend Fold

6.1. Model Description

[37] We present a two-dimensional numerical landscape evolution model that predicts landscape elevation, h, as a function of horizontal locations, x and y, and time, t. Model behavior is governed by a set of equations for tectonic displacement of bedrock and erosion. Without much loss of generality, we can consider the case of a classic fault-bend fold in which a hanging wall of thickness T moves laterally above a horizontal detachment at constant speed, V, and then up a ramp with dip α (Figure 13) [*Suppe*, 1983]. This rule adequately predicts deformation in many fold-and-thrust belts over periods greater than a single seismic cycle [e.g., *Suppe*, 1983; *Shaw and Suppe*, 1996; *Mugnier et al.*, 1999; *Lavé and Avouac*, 2000]. Fault slip rate is equivalent to V. The ramp strikes in the y direction. The upper tip of this ramp is set to the initial elevation of the model surface, which is the local erosional base level, at which the fault bends back into a horizontal flat. Bedrock streamlines parallel the fault following a simple kinematic function that preserves line length and conserves mass. As bedrock passes over the ramp, also with velocity V, the hanging wall is deformed in a kink band between planar axial surfaces with dips β that project from the flat-ramp–flat-intersections. Axial surface dip, β, is defined as $\beta = (180 - \alpha)/2$. Velocities change direction, but not magnitude, across axial surfaces. Above the fault ramp and between the two active axial surfaces, bedrock velocity components are functions of ramp dip α as seen in (9) and (10).

[38] Erosion in the model consists of stream incision proportional to unit stream power and hillslope proportional to topographic curvature. In effect, the surface process rules used in the model represent end-member processes for topographic relief production and topographic smoothing. As in the previous section, the fluvial erosion rate in bedrock channels is computed using the unit stream power equation, $E = KA^{1/2}S$. Stream erosion is assumed to be detachment-limited and therefore sediment is not explicitly transported or deposited.

[39] Hillslope erosion is simulated with an equation for linear diffusion in two horizontal dimensions [*Culling*, 1965],

$$E = -\kappa\left(\frac{\partial^2 h}{\partial x^2} + \frac{\partial^2 h}{\partial y^2}\right), \tag{13}$$

where κ is a spatially constant diffusivity ($m^2 \cdot a^{-1}$). This relation has been shown to reasonably predict sediment erosion rates in regolith-mantled landscapes where soil creep occurs [e.g., *McKean et al.*, 1993; *Roering et al.*, 2002]. Our model assumes that regolith is produced at the same rate as erosion. Hillslope creep is not necessarily widespread in active orogens, where erosion rates outpace regolith production rates and landsliding is common owing to steep topographic slopes. However, the distinction among these hillslope sediment transport rules is a second-order detail for the purposes of our analysis. In the same spirit as our treatment of streams, diffusion-like processes erode but do not explicitly deposit sediment, which is assumed to quickly enter the fluvial system and exit the model space.

[40] Combining the unit stream power equation and (13) with a tectonic velocity field that ignores internal shortening yields a continuity equation for landscape evolution,

$$\frac{\partial h}{\partial t} = u + v\frac{\partial h}{\partial x} + \kappa\left(\frac{\partial^2 h}{\partial x^2} + \frac{\partial^2 h}{\partial y^2}\right) - KA^{1/2}S. \tag{14}$$

To facilitate analysis, we nondimensionalize (14) as

$$\frac{\partial h^*}{\partial t^*} = u^* + v^*\frac{\partial h^*}{\partial x^*} + \frac{\kappa}{TV}\left(\frac{\partial^2 h^*}{\partial x^{*2}} + \frac{\partial^2 h^*}{\partial y^{*2}}\right) - \frac{KT^{2m}}{V}A^{*1/2}S, \tag{15}$$

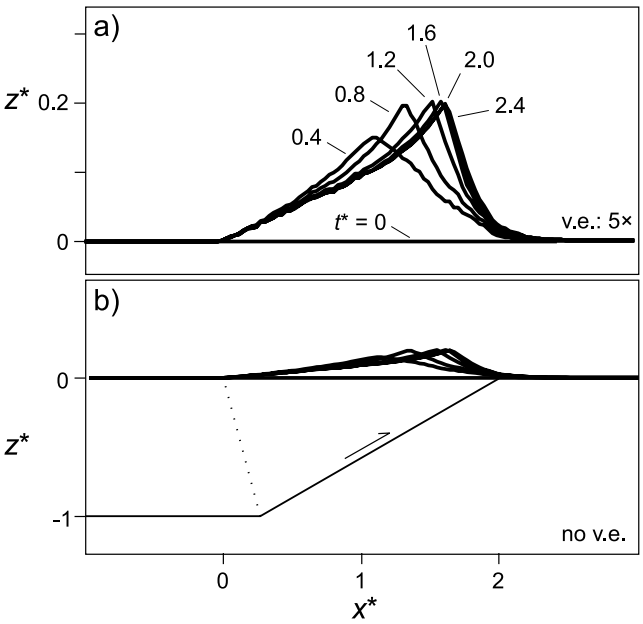

Figure 14. Topographic profiles (a) with and (b) without vertical exaggeration during the approach toward topographic and flux steady states. The fault is also shown in Figure 14b. Topographic profiles are shown at $t^* = 0$, 0.4, 0.8, 1.2, 1.6, 2.0, and 2.4. Topographic profiles shown are the minimum elevations measured in the y direction and therefore closely represent paired stream long profiles. Model parameters are $N_e = 5$, $D = 0$, and $\alpha = 30°$.

which can be written

$$\frac{\partial h^*}{\partial t^*} = \sin\alpha + \cos\alpha \frac{\partial h^*}{\partial x^*} + D\left(\frac{\partial^2 h^*}{\partial x^{*2}} + \frac{\partial^2 h^*}{\partial y^{*2}}\right) - N_e A^{*1/2} S. \tag{16}$$

[41] Definitions of the nondimensional variables are given in Appendix A.

[42] As evident in (16) and following *Willett et al.* [2001], model behavior is controlled by three nondimensional parameters: a diffusion number (D), a fluvial erosion number (N_e), and ramp dip (α). These parameters have physical significance. The diffusion number, $D = \kappa/TV$, is the inverse of the typical Péclet number and thus represents the efficacy of erosional flux by diffusion-like processes versus tectonic flux. Likewise, the fluvial erosion number, $N_e = KT^{2m}/V$, represents the efficacy of fluvial erosional flux versus tectonic flux. Variations in tectonic forcing rates are therefore equivalent to variations in erosivity.

[43] Solutions to (16) are obtained using CHILD, a finite-volume landscape evolution model that operates on an irregular grid [*Tucker et al.*, 2001]. Lateral displacement of bedrock and topography at each time step is simulated by including an apparent uplift component at each node, the second term on the right side of (14)–(16). In our model, the average nondimensional horizontal node spacing is 0.5 and the simulation space is 8 units long in the y direction, parallel to fault strike. All four model boundaries are open to flow. Both fluvial and hillslope erosion are computed at every node. Finally, we assume steady and uniform precipitation, bedrock erodibility, diffusivity, and fault slip rates. All simulations were run to flux steady state, when erosional efflux equals tectonic influx [*Willett and Brandon*, 2002]. Numerical experiments were designed to investigate cross sections of realistic parameter space rather than completely explore parameter space. In three sets of experiments, we explore the response of steady state model topography to variations in ramp dip, fluvial erosion number, and diffusion number.

6.2. Results

6.2.1. Topographic Response to Different Ramp Dips

[44] First, for a reference model in which $\alpha = 30°$, topography in early time steps ($t^* < 0.4$) is nearly symmetrical (Figure 14). By $t^* \approx 0.8$, the ridge reaches its maximum elevation but is not yet at steady state. The ridge's profile becomes increasingly asymmetrical until steady state is reached at $t^* \approx 2.0$. The slope-area data from this model are consistent with the 1-D model (not shown).

[45] As expected from the simple analytical model, the 2-D model ridge varies in asymmetry as a function of ramp dip (Figure 15). Rock flux and erodibility are kept constant in all cases by setting N_e constant ($N_e = 10$ in Figure 15) but maximum elevations are achieved when ramp dip is vertical ($\alpha = 90°$), demonstrating that total relief is tied to the vertical component of the bedrock flux. Also, the ridge is symmet-

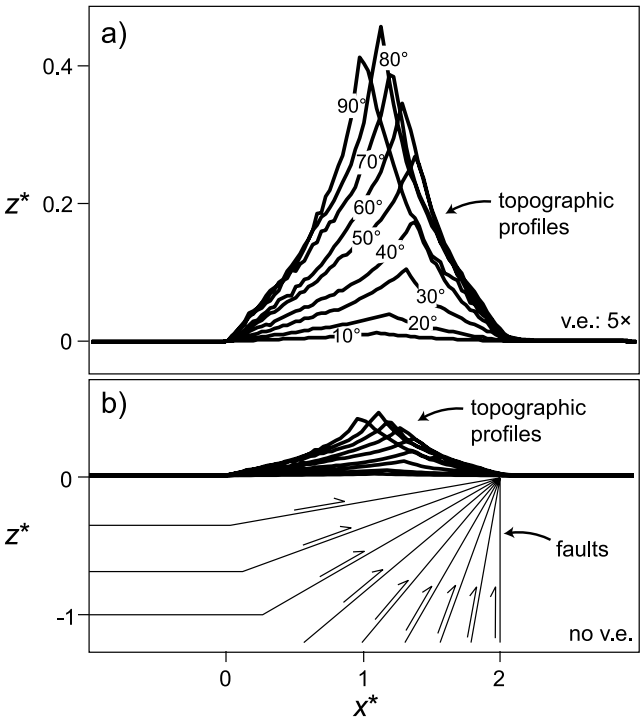

Figure 15. Steady state topographic profiles (a) with and (b) without vertical exaggeration for models with different ramp dips, α. Greatest cross-range asymmetry is achieved when $\alpha = 45°$. Profiles shown are minimum elevations measured in the y direction. Model parameters are $N_e = 10$ and $D = 0$. To maintain a constant range width, T increases with α.

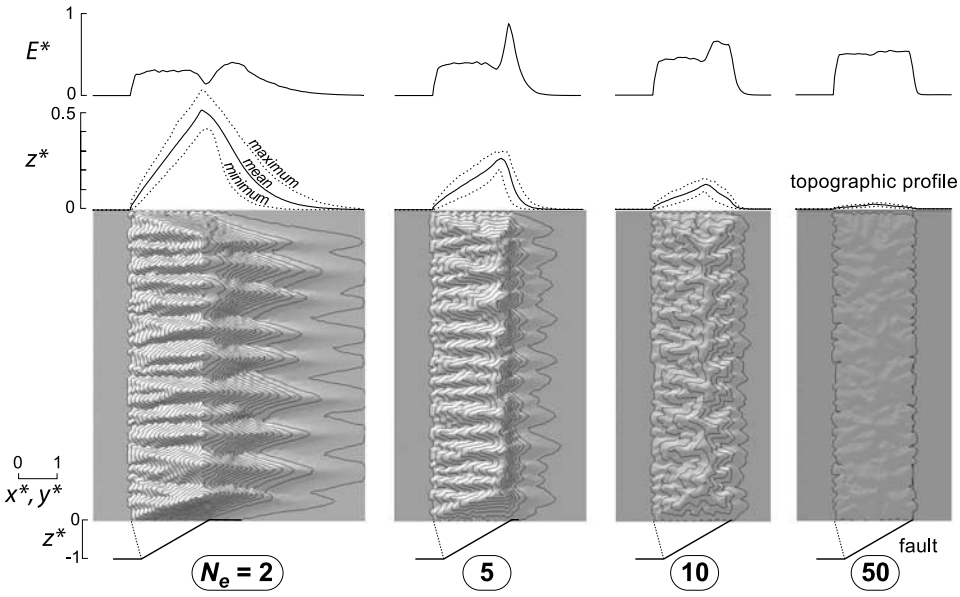

Figure 16. Four simulations in which fluvial erosion number is varied (N_e = 2, 5, 10, and 50). Contour maps show nondimensional elevation, h^*. Nondimensional erosion rates, E^*, topographic swath profiles, and fault geometry are shown. D and α are constant (D = 0, α = 30°). Vertical exaggeration of topographic profiles is 5×. Contour interval is 0.04.

rical when ramp dip is vertical, where erosional flux is independent of topographic slope. The ridge is also nearly symmetrical when ramp dip is very low: slopes are gentle because rock uplift is minimal, which leads to erosion rates being nearly uniform, which in turn drives slopes to be similar. Maximum asymmetry is achieved at intermediate ramp dips (α = 45°).

6.2.2. Topographic Response to Different Fluvial Erosion Numbers

[46] At large N_e, the steady state ridge is low in elevation and nearly symmetrical (Figure 16). Erosion rates are also nearly equal on both ridge flanks. At lower N_e, asymmetry in topographic profile and erosion rates increases to a maximum at $N_e \approx 5$. At this point the ridge crest becomes pinned to the active upper axial surface and the proximal ridge flank attains its maximum width. Lowering N_e further, however, results in the hanging wall extending out over the upper flat. In the kink band above the upper flat, u = 0. Without rock uplift to increase relief and topographic slopes in this region, streams must increase drainage areas in order to adjust erosion rates. Therefore the distal flank lengthens and the sense of asymmetry reverses. At lower fluvial erosion numbers, total relief increases (total relief → T as $N_e \rightarrow 0$), and valleys become straighter and aligned. At extremely low fluvial erosion numbers, distal stream profiles develop convex reaches near their heads where proximal streams are advected across the drainage divide and to the distal side.

6.2.3. Topographic Response to Different Diffusion Numbers

[47] In the first set of simulations, the efficacy of diffusion-like processes is investigated in the presence of fluvial erosion. Fluvial erosion number and ramp dip are fixed (N_e = 10 and α = 30°) and diffusion number varied over 3 orders of magnitude (D = 0.001–1). Over most of this range, erosion is dominantly fluvial and diffusion does not visibly affect the asymmetry of the range, although diffusion does decrease local relief as seen in the difference between maximum and minimum elevation profiles (Figure 17). Visible hillslope smoothing is noticeable where $D > 0.1$, owing to higher diffusivities and/or shorter effective horizontal dimensions being simulated (because ridge width is a function of T). Where D is within ~2 orders of magnitude of N_e, range asymmetry, as quantified by w_d/w_p, is equally sensitive to both parameters (Figure 18a). For the CHILD simulations, w_d/w_p is measured from the minimum elevation profile (shown in Figures 16 and 17) and the ridge is operationally defined as occurring where $h^* \geq 0.001$. Where $N_e \gg D$, however, fluvial erosion controls drainage divide position and therefore the range's steady state topographic asymmetry.

[48] In the second set of simulations, fluvial erosion is absent (N_e = 0), ramp dip is constant (α = 30°), and diffusion number is increased (D = 1–100). Interestingly, topography with $w_d/w_p > 1$ occurs in all simulations (Figure 18b). Where stream erosion is present, $w_d/w_p > 1$ only occurs when fluvial erosivity is low or bedrock velocity is fast ($N_e \leq 4$).

6.2.4. Comparison to the Siwalik Hills

[49] Parameters appropriate for the Siwalik Hills were estimated for comparison with model results (Appendix B). Fluvial erosion number falls in a likely range between 5 and 40. Diffusion number is ≤1. Fault ramps generally dip 30°–60°. On the basis of the location of the fluvial-colluvial transition, interpreted to occur at the bend in the slope-area plot [*Montgomery and Foufoula-Georgiou*, 1993], colluvial valleys and hillslopes centered about the ridge pole constitute only a small fraction (<10%) of the total width of the Siwalik Hills, suggesting that topographic asymmetry here should indeed be more sensitive to stream profile shape than hillslope form. For this reason and because diffusion has

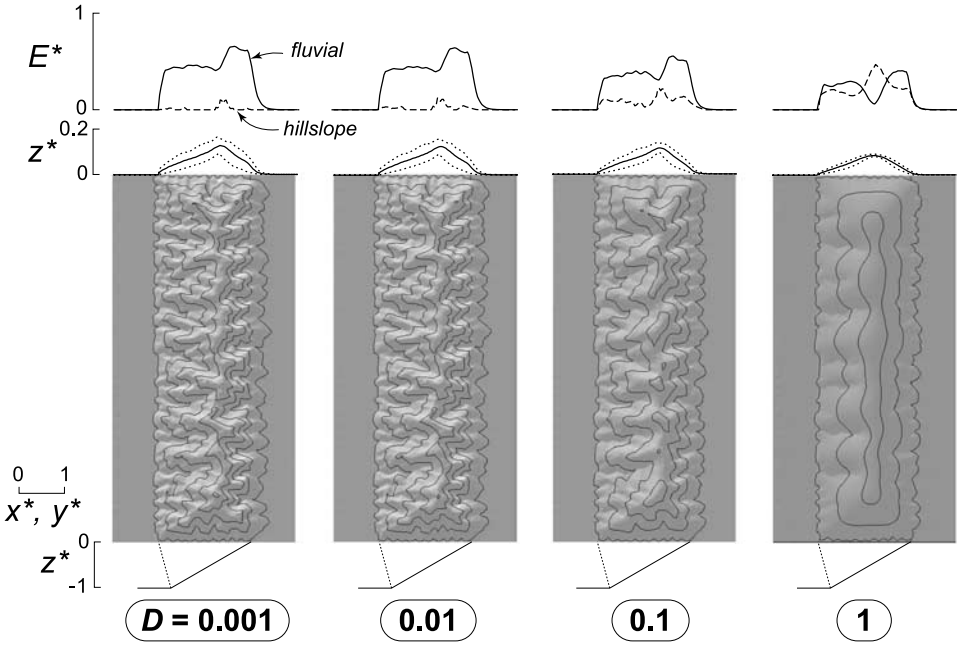

Figure 17. Four simulations in which diffusion number is varied (D = 0.001, 0.01, 0.1, and 1). Contour maps show nondimensional elevation, h^*. Nondimensional erosion rates, E^*, topographic swath profiles, and fault geometry also shown. Fluvial (solid line) and hillslope (dashed line) components of erosion are shown. N_e and α are constant (N_e = 10, α = 30°). Vertical exaggeration of topographic profiles is 5×. Contour interval is 0.04.

little effect on model topography except when D is large or N_e very low, diffusion-like processes can be ignored in our comparison of model and Siwalik Hills fault-bend fold topography.

[50] The numerical landscape evolution model satisfactorily reproduces the general topographic characteristics of the Siwalik Hills with fluvial incision as the dominant erosion process and for a straight ramp with intermediate dip. Range height and drainage divide position are reasonably predicted by a range of fluvial erosion numbers (N_e = 5–15) (Figure 19). This threefold range of fluvial erosion numbers is expected from the nearly three-fold range of normalized steepness indices observed among these sites. Inclusion of a curved ramp in the model simulations would lead to different results but we suggest that results of a straight ramp highlight the first-order topographic predictions of fault-bend folding and lateral advection.

7. Discussion

7.1. Lateral Bedrock Motion and Stream Profiles

[51] As demonstrated above, steady state stream profiles above fault-bend folds vary in shape, as reflected in concavity and steepness indices, systematically with the direction of tectonic vergence. Importantly, model results show that lateral advection is expected to affect the form of slope-area plots in ways not expected owing to vertical rock uplift alone. These indices demand careful interpretation, as other factors may affect the concavity index, including spatial gradients in rock uplift rate [*Kirby and Whipple*, 2001], bedrock resistance to erosion [*Duvall et al.*, 2004], and orographic precipitation [*Roe et al.*, 2002]. The role of rock uplift rate gradients was discussed already in section 5.2.3; the possible effects of the latter two are discussed below.

[52] Distal streams analyzed tend to flow across the Lower Siwalik unit whereas proximal streams tend to flow across the Middle Siwalik unit. The difference in erodibility between and within these units is not well known, but previous work in the eastern site has not shown the difference to be significant [*Kirby and Whipple*, 2001] and therefore we do not attribute the differences in steepness or concavity on the two flanks to lithology.

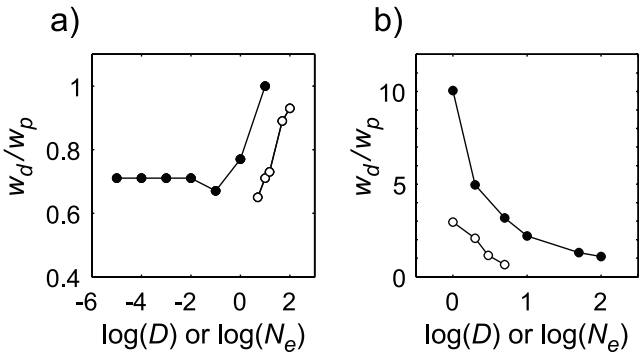

Figure 18. Plots showing the relations between ridge position, as indicated by the ratio of distal and proximal ridge widths, w_d/w_p. Black circles show simulation results where diffusion number is varied and fluvial erosion number is constant (N_e = 10 in Figure 18a and N_e = 0 in Figure 18b). Open circles show simulations where diffusion number (D = 0) is constant and N_e is varied. Ramp dip is 30° in all simulations.

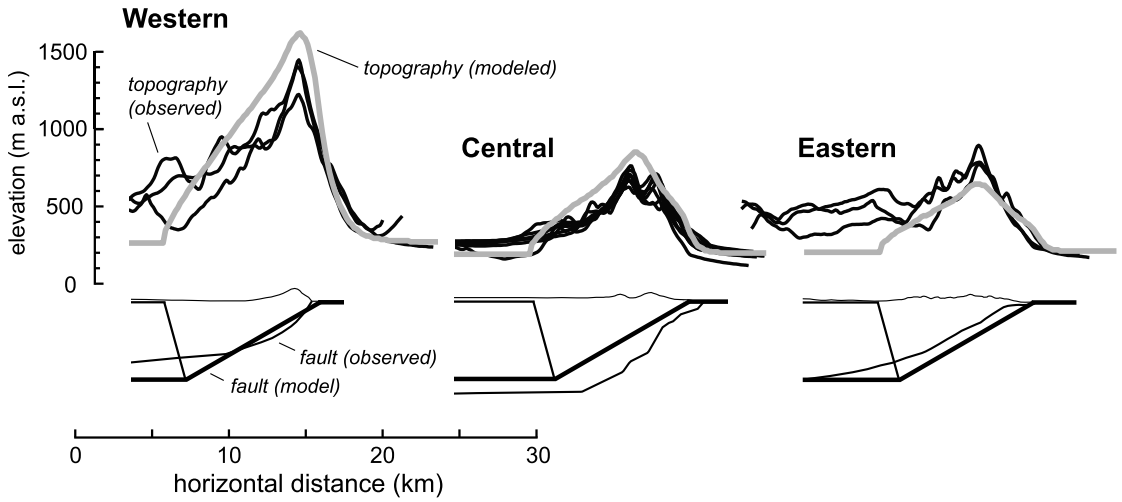

Figure 19. (top) Topographic profiles of the Siwalik Hills (black) and the model (gray). Profiles represent mean elevations along swaths 5 km wide. (bottom) Cross sections for the Siwalik Hills and the model. Model profiles are mean elevations measured in the y direction. Siwalik Hills profiles are mean elevations calculated over 5-km-wide swaths. Vertical exaggeration of the topographic profiles is 10×. Cross sections are not vertically exaggerated. Model parameters are $\alpha = 30°$, $N_e = 5$, 10, and 15 (west to east), and $D = 0$. Choice of model parameter N_e estimated from local steepness indices, which increase from east to west. The western cross section is the closest to the western topographic profiles but hanging wall thicknesses and fault geometries may be expected to differ between sites. See Figure 1 for locations.

[53] The total relief in the Siwalik Hills, which is as much as ~1300 m, is likely to produce orographic precipitation, with greater precipitation falling on the windward side of the range [*Smith*, 2006]. Whereas there is a band of high precipitation rates over the frontal portion of the Himalaya consistent with rain-out over the Siwalik Hills [*Bookhagen et al.*, 2005; *Anders et al.*, 2006] and greater precipitation rates might be expected on the southern flanks of the range, gradients across the Siwalik Hills have not been established owing to the coarse spatial resolution of the cited satellite-based measurements (~10 km). However, previous models have shown that stream slopes should be gentler on the wet sides of mountain ranges [*Beaumont et al.*, 1992], which is inconsistent with steepness indices measured. Similarly, orographic precipitation is expected to impart variations in profile concavity. On the basis of models of orographic precipitation and steady state detachment-limited stream profiles, θ varies from 0.4 to 0.6 for model parameter ratio $m/n = 0.5$ [*Roe et al.*, 2002], similar to what can be expected from lateral advection. Values of θ less than 0.5 reflect precipitation rates increasing toward the channel head whereas values greater than 0.5 reflect precipitation rates decreasing away from the channel head. Despite uncertainty in the precipitation pattern, we contend that the steepness and concavity indices observed in the Siwalik Hills are more consistent with numerical models of fault-bend folding rather than orographic precipitation.

[54] The least ambiguous evidence for lateral advection having an effect on steady state geomorphology is expected to occur on hillslopes and in colluvial valleys because their steep slopes and short length scales, which make their morphologies less complicated by gradients in rock uplift rate or changes in lithology. One might expect lateral bedrock motion to impact colluvial valley geomorphology, which has been shown locally to follow a stream-power functional form [*Lague and Davy*, 2003]. Certainly, the response of hillslopes to lateral advection merits further study.

[55] The role of hillslopes in fluvial incision has been ignored in the current study but also deserves attention. The sensitivity of sediment production on hillslopes is thus expected to make fluvial geomorphology even more sensitive to lateral advection than simulated in this paper, if one incorporates sediment-flux-dependent incision rules [*Whipple and Tucker*, 2002; *Gasparini et al.*, 2006; *Crosby et al.*, 2007; *Gasparini et al.*, 2007]. One prediction of landscape evolution models with sediment-flux-dependent incision is the production of oversteepened reaches [*Gasparini et al.*, 2006; *Crosby et al.*, 2007]. Such steep reaches of streams have been observed to reach slopes up to $S \approx 1$ [*Schoenbohm et al.*, 2004; *Gasparini et al.*, 2006; *Wobus et al.*, 2006b; *Crosby et al.*, 2007]. Like hillslopes, the responses of these oversteepened reaches may be affected considerably by lateral advection.

[56] Interestingly, some slope-flux-dependent incision models also produce steady state slope-area plots that have steeper apparent concavities than expected by the unit stream power model [*Gasparini et al.*, 2007], and such models also show transient responses may also exhibit large concavities corresponding with large steepness indices [*Gasparini et al.*, 2006]. Such large concavities have not been noted in streams that flow in the strike-parallel direction [*Kirby and Whipple*, 2001] and thus the importance of sediment-flux-dependent incision in the Siwalik Hills remains unclear.

[57] We contend that stream profiles can be used to assess qualitatively the bedrock deformation field that underlies them, particularly if spatial patterns of precipitation are reasonably known, such as by satellite [*Bookhagen et al.*, 2005; *Anders et al.*, 2006]. Given the noise common in

slope-area data and the other factors discussed, steepness and particularly concavity indices, alone, may not provide reliable evidence of lateral advection. Instead, a qualitative comparison of slope-area plots for paired proximal and distal streams is probably more useful and informative. Although the effects of ramp dip and erosivity may be similar, we have demonstrated how to establish the presence of lateral bedrock motion by analyzing stream channel data at low drainage areas. This could be used to help differentiate, for example, active from inactive fault-bend folds where more direct data are scarce. In contrast, the profile shapes of reaches downstream from the principal drainage divide may allow us to determine whether fault ramps are curved or straight.

7.2. Cross-Range Topographic Asymmetry

[58] For the simple deformation characteristics of a classic fault-bend fold and for the relatively small size common among such folds, lateral bedrock motion and erosion are sufficient to cause steady state topography to be asymmetrical. A classic fault-bend fold does not create such asymmetry in the absence of erosion: instead, a constantly widening plateau forms and the width of its distal slope is set by the axial surface dip and upper flat dip. More specifically, the sense of asymmetry observed in the Siwalik Hills ($w_d/w_p < 1$) was only replicated by simulations when fluvial erosion was active. This sense of asymmetry is also observed above other active fault-bend folds, such as above the Chutouchi and Pingchi faults in the tectonically active Western Foothills of Taiwan [*Hickman et al.*, 2002], an area that may also be in approximate steady state [*Hsieh and Knuepfer*, 2002].

[59] Our models show that asymmetry arises because of a low erosional efficiency of streams and/or a high rate of lateral advection relative to rock uplift. The ridge-flank width ratio is minimized at intermediate fault dips (α = 45°) because of a compromise between rock uplift and lateral advection: rock uplift is necessary for developing relief and steep slopes, whereas steep slopes are the most sensitive to lateral advection. Advection of topography across convergent mountain ranges, another potential consequence of lateral bedrock advection, is also maximized at intermediate fault dips for similar reasons [*Miller and Slingerland*, 2006].

[60] For a fault-bend fold geometry, diffusion alone appears incapable of creating a range that is steeper on the front that on the back. Diffusion alone, both in our simulations with a fixed ramp dip and no fluvial erosion (Figure 14b), and those of *Leturmy et al.* [1995], produces a reversed sense of asymmetry in which $w_d/w_p > 1$, as hanging walls advance out over an upper flat. Model topography with reverse asymmetry also occurs at very low fluvial erosion numbers. Advances of mountain ranges over upper flats may reflect changes in climate or fault slip rate and be observable in the rock record [*De Paor and Anastasio*, 1987; *Burbank and Beck*, 1991].

[61] Our observations that fluvial erosion dominates the asymmetric form of model topography under realistic parameters are in agreement with *Herman and Braun* [2006]. Others have argued that hillslope diffusion should dominate on ridge lines and therefore control their migration [*Willett et al.*, 2001]. However, whereas stream erosion does not directly erode ridge lines, it does set the lower boundary condition for, and thus drive erosion on, adjacent hillslopes. Reiterating an earlier point, the role of hillslope erosion on fault-bend fold topography may become more significant as we incorporate sediment-flux-dependent stream incision rules into simulations of fault-bend folds.

[62] Past modeling studies have shown that topographic profile asymmetry can also arise owing to spatial gradients in rock uplift rate [e.g., *Kuhni and Pfiffner*, 2001; *Schlunegger et al.*, 2001], internal shortening [*Willett et al.*, 2001], orographic precipitation [*Beaumont et al.*, 1992; *Batt and Braun*, 1999; *Willett*, 1999; *Herman and Braun*, 2006], and from the internal frictional properties and fault geometries of critical wedges [*Koons*, 1990; *Carena et al.*, 2002; *Whipple and Meade*, 2004]. Therefore the cause of asymmetry in real mountain ranges must be interpreted with caution. Orographic precipitation, for example, can alter the degree of asymmetry and even reverse it but such precipitation patterns are not a necessary condition for it. In the case of critical wedges, asymmetry is insensitive to erosional and tectonic boundary conditions (K and V, respectively) but is instead a function of underlying fault geometry [e.g., *Carena et al.*, 2002]. Numerical models with internal horizontal shortening show that asymmetry arises in the absence of erosion, suggesting that erosion tends to make the mountain range more symmetrical as well as maintain steady state [*Willett et al.*, 2001]. In the model of *Willett et al.* [2001], in which no lateral bedrock displacement is allowed beyond top of the ramp, the model mountain range becomes increasingly asymmetrical as N_e goes to 0. Ridge-flank width ratios greater than 1 do not occur. Both results contrast with our fault-bend fold model and largely reflect different boundary conditions.

[63] Analytical results of the present study are consistent with past studies that show spatially varying uplift rates, such as those above a curved ramp, can also produce asymmetrical ridges. However, the degree of asymmetry is only sensitive to convergence velocity and climate (ignoring orographic precipitation) if the model also accounts for lateral advection. As noted by *Herman and Braun* [2006], changes in climate or tectonic forcing are expected to affect asymmetry. They observe that as one proceeds southwestward along the Southern Alps of New Zealand, the convergence rate across the Alpine Fault decreases and the distance between the fault and the range divide increases, consistent with their model predictions that asymmetry decreases with as V decreases (or N_e increases). For similar reasons, we suggest that the westward increase in steepness and concavity indices in the Siwalik Hills, as well as an increase in the front-to-back differences in these indices, could be due to a westward decrease in the precipitation rate at the Himalayan front as easterly monsoonal storm tracks rain out [*Bookhagen et al.*, 2005] but it could also be due to along-strike changes in fault geometry, including dip or curvature. It is not likely to be the result of a westward increase in fault slip rate, which would have to be by a factor of 3 to produce the same change in asymmetry. In fact, Quaternary slip rates on the Main Frontal thrust appear to decrease slightly westward, where recent slip may be partitioned with the Main Dun thrust [*Mugnier et al.*, 2004]. Also, along-strike changes in fault dip, between 30° and 60° for example, would increase k_{sn} by less than a

factor of 2 and therefore cannot account entirely for the observed westward increase in steepness indices and cross-range asymmetry.

8. Conclusions

[64] This study set out to determine if lateral advection leaves a topographic fingerprint, particularly in fluvial topography such as bedrock stream longitudinal profiles. Its secondary goal was to assess what processes likely control steady state asymmetry of mountain range profiles in the cross-strike direction, or what processes are likely to drive drainage divide migration.

[65] Model simulations predict several diagnostic consequences of lateral bedrock advection on fluvial topography formed above fault-bend folds. Such bedrock motion is a sufficient condition to cause (1) greater concavity and steepness indices for detachment-limited streams that flow in the direction of lateral advection than for streams that flow in the opposite direction; (2) asymmetry of cross-range topographic profiles; and (3) asymmetry in erosion rates across the principal drainage divide, with faster rates on the distal flank. Lateral advection is also a necessary condition for differences observed in steepness and concavity indices in paired proximal and distal low-order streams near the principal drainage divide, where vertical rock uplift rate and lithology are not likely to vary much. Measurements of stream channels and topographic profiles from active fault-bend folds in the Siwalik Hills, Nepal, are consistent with these model predictions. Our analyses thus show that the tectonic velocity field beneath detachment-limited stream profiles must be interpreted cautiously because lateral advection in a uniform velocity field can impart variations in stream steepness similar to those due to spatial variations in rock uplift rate.

[66] Next, model results and observations from the Siwalik Hills indicate that drainage divide position in mountain ranges (or settings with length scales larger than the hillslope length), for reasonable erosion parameters, is governed by fluvial processes rather than the suite of hillslope processes that exhibit diffusion-like behavior. Topographic asymmetry is expected to be sensitive to along-strike variations in precipitation rate, fault slip rate, or ramp dip or temporal changes in any of these variables.

[67] The geomorphologic community's understanding of the factors affecting stream profiles and the caveats these factors pose for interpretation continue to increase. Bearing other factors in mind, steep streams hold potentially useful information about lateral as well as vertical components of deformation. In settings where bedrock velocities are great, bedrock erodibility is low, or precipitation rates are low, lateral advection is expected to have a significant topographic signal and should be accounted for in tectonic geomorphologic analyses.

Appendix A: Equations for Nondimensional Variables and Parameters

[68] Spatial variables

$$x^* = \frac{x}{T},\ y^* = \frac{y}{T},\ z^* = \frac{z}{T},\ h^* = \frac{h}{T},\ A^* = \frac{A}{T^2}, \tag{A1}$$

Velocity

$$u^* = \frac{u}{V},\ v^* = \frac{v}{V}, \tag{A2}$$

Time

$$t^* = \frac{tV}{T}, \tag{A3}$$

Erosion rate

$$E^* = \frac{E}{V}, \tag{A4}$$

Erosional parameters

$$D = \frac{\kappa}{TV},\ N_e = \frac{KT^{2m}}{V}. \tag{A5}$$

Appendix B: Estimation of Nondimensional Parameters for the Siwalik Hills

[69] For comparison against the model results, one must consider where the Siwalik Hills lie in parameter space. Ramp dip, N_e, and D are all known or can be estimated from existing calculations. The MFT and MDT have average ramp dips (α) beneath the study sites ranging from 30° to 45°, although ramps can reach local maxima of ~60° [*Mugnier et al.*, 1999; *Lavé and Avouac*, 2000]. Hanging wall thickness (T) ranges from 4 to 6 km [*Mugnier et al.*, 1999; *Lavé and Avouac*, 2000]. Holocene fault slip rates on the MFT are 13–17 mm/a in central Nepal [*Mugnier et al.*, 2004] and 21–22 mm/a in eastern Nepal [*Lavé and Avouac*, 2000]. These measurements are consistent with slip rates farther west on the MFT near Dehra Dun of 14 mm/a [*Wesnousky et al.*, 1999]. Measured Holocene fault slip rates on the MDT in central-western Nepal are ~4 mm/a [*Mugnier et al.*, 2004].

[70] Erosion parameters have been estimated in the eastern Nepal study area on the basis of the likelihood that the Siwalik Hills are in a flux and topographic steady state [*Hurtrez et al.*, 1999]. The mass diffusivity calculated for hillslopes is $\kappa = 9.3 \pm 0.5$ m^2/a (2σ) [*Hurtrez et al.*, 1999]. Given $T \approx 5$ km and $V \approx 0.02$ m/a, then $D \approx 0.1$. Constraints on κ at other sites are lacking, but given the range in T and V, we expect D to vary over less than 1 order of magnitude ($D \approx 0.08$–0.6). It should be noted, however, that this value of diffusivity is much larger than those estimated for soil creep and other diffusion-like processes that have been measured at the hillslope scale where κ ranges from 10^{-2} to 10^{-4} m^{2}a^{-1} [see *Martin and Church*, 1997; *Martin*, 2000]. Diffusivity calculated for hillslopes experiencing episodic landslides tends to be ~10^{-1} m^{2}a^{-1} [*Martin*, 2000]. The much higher estimates for the Siwalik Hills, estimated at a much larger length-scale than a single hillslope, suggest that nondiffusive processes are being included. Although landslides are common in the Siwalik Hills [*Hurtrez et al.*, 1999], we suggest that a realistic diffusion number is likely ≤ 1.

[71] In the eastern region, near the Bakeya and Bagmati Rivers, estimates of K fall between 1.47×10^{-4} and 1.64×10^{-4} $m^{0.08}/a$ when $m = 0.46$ [*Kirby and Whipple*, 2001]. Mean annual precipitation varies substantially across southern Nepal by a factor of ~4, indicating that the above value of K should also vary spatially, ignoring other factors such as lithology [*Bookhagen et al.*, 2005]. The eastern study area lies in a region of high precipitation rates relative to much of southern Nepal. Given that K scales with precipitation rate to a power of ~1/2, we might expect that K should vary owing to precipitation by a factor of ~2. Bearing in mind that V and K are probably the least well-constrained parameters among our three sites, N_e likely falls between approximately 5 and 125. Considering that our sites are mostly over the more active MFT, our preferred range of N_e is 5–40. The ratio K/V probably varies from 0.001 to 0.008.

Notation

A drainage area, m^2.
$A_{\min}$ minimum steady state drainage area on distal ridge flank, m^2.
A^* nondimensional drainage area, unitless.
D diffusion number, unitless.
E erosion rate, m a^{-1}.
E^* nondimensional erosion rate, unitless.
h elevation of land surface, m.
h^* nondimensional elevation of land surface, unitless.
k_s empirical slope-area relation coefficient, $m^{2\theta}$.
k_{sn} normalized empirical slope-area relation coefficient, or steepness index, $m^{2\theta}$.
k_x area-length coefficient, $m^{(2-\eta)}$.
K stream power coefficient, m^{1-2m} a^{-1}.
m area exponent in stream-power equation, unitless.
n slope exponent in stream power equation, unitless.
N_e fluvial erosion number, unitless.
S stream channel bed gradient, unitless.
$S_{\max}$ maximum steady state slope on proximal ridge flank, unitless.
t time, annums.
t^* nondimensional time, unitless.
T thickness of fault-bend fold hanging wall or plateau-margin extrusion block, m.
u vertical component of bedrock velocity, m a^{-1}.
u^* nondimensional vertical component of bedrock velocity, unitless.
v horizontal component of bedrock velocity, m a^{-1}.
v^* nondimensional horizontal component of bedrock velocity, unitless.
V hanging wall velocity, m a^{-1}.
w_d distal ridge-flank width, m.
w_p proximal ridge-flank width, m.
x, y horizontal dimensions, m.
x^*, y^* nondimensional horizontal dimensions, unitless.
z vertical dimension, m.
z^* nondimensional vertical dimension, unitless.
α ramp dip, deg.
β axial surface dip, deg.
η area-length (Hack) exponent, unitless.
θ empirical slope-area relation exponent, or concavity index, unitless.
θ_{ref} reference concavity index, unitless.
κ diffusivity, m^2 a^{-1}.
σ topographic slope in x-direction, deg.

[72] **Acknowledgments.** This research was done while S. R. M. was partially supported by a Shell Foundation Doctoral Fellowship and by NSF grant OCE-0548387 awarded to R. L. S. S. R. M. would like to thank J. Barton, D. Edmonds, and J. Lock for helpful discussions and R. Alley, D. Fisher, and M. Gahegan for insightful comments on early versions of this manuscript. Thorough reviews by M. Attal, C. Wobus, and Associate Editor G. Tucker improved this manuscript.

References

Adams, J. (1980), Contemporary uplift and erosion of the Southern Alps, New Zealand, *Geol. Soc. Am. Bull.*, *91*, 1–114.

Adams, J. (1985), Large-scale tectonic geomorphology of the Southern Alps, New Zealand, in *Tectonic Geomorphology*, edited by M. Morisawa and J. T. Hack, pp. 105–128, Allen and Unwin, London.

Anders, A. M., et al. (2006), Spatial patterns of precipitation and topography in the Himalaya, in *Tectonics, Climate, and Landscape Evolution*, edited by S. D. Willett et al., *Spec. Pap. Geol. Soc. Am.*, *398*, 39–53.

Attal, M., and J. Lavé (2006), Changes of bedload characteristics along the Marsyandi River (central Nepal): Implications for understanding hillslope sediment supply, sediment load evolution along fluvial networks, and denudation in active orogenic belts, in *Tectonics, Climate, and Landscape Evolution*, edited by S. D. Willett et al., *Spec. Pap. Geol. Soc. Am.*, *398*, 143–171.

Barros, A. P., et al. (2006), From weather to climate—Seasonal and interannual variability of storms and implications for erosion processes in the Himalaya, in *Tectonics, Climate, and Landscape Evolution*, edited by S. D. Willett et al., *Spec. Pap. Geol. Soc. Am.*, *398*, 17–38.

Batt, G. E., and M. T. Brandon (2002), Lateral thinking: 2-D interpretation of thermochronology in convergent orogenic settings, *Tectonophysics*, *349*, 185–201.

Batt, G. E., and J. Braun (1999), The tectonic evolution of the Southern Alps, New Zealand: Insights from fully thermally coupled dynamical modelling, *Geophys. J. Int.*, *136*, 403–420.

Beaumont, C., et al. (1992), Erosional control of active compressional orogens, in *Thrust Tectonics*, edited by K. R. McClay, pp. 1–18, Chapman and Hall, London.

Beaumont, C., et al. (2001), Himalayan tectonics explained by extrusion of a low-viscosity crustal channel coupled to focused surface denudation, *Nature*, *414*, 738–742.

Beaumont, C., R. A. Jamieson, M. H. Nguyen, and S. Medvedev (2004), Crustal channel flows: 1. Numerical models with applications to the tectonics of the Himalayan-Tibetan orogen, *J. Geophys. Res.*, *109*, B06406, doi:10.1029/2003JB002809.

Bilham, R., et al. (1997), GPS measurements of present-day convergence across the Nepal Himalaya, *Nature*, *386*, 61–64.

Bollinger, L., J. P. Avouac, O. Beyssac, E. J. Catlos, T. M. Harrison, M. Grove, B. Goffé, and S. Sapkota (2004), Thermal structure and exhumation history of the Lesser Himalaya in central Nepal, *Tectonics*, *23*, TC5015, doi:10.1029/2003TC001564.

Bookhagen, B., et al. (2005), Abnormal monsoon years and their control on erosion and sediment flux in the high, arid Northwest Himalaya, *Earth Planet. Sci. Lett.*, *231*, 131–146.

Burbank, D. W., and R. S. Anderson (2001), *Tectonic Geomorphology*, 274 pp., Blackwell Sci., Oxford, U.K.

Burbank, D. W., and R. A. Beck (1991), Rapid, long-term rates of denudation, *Geology*, *19*, 1169–1172.

Carena, S., et al. (2002), Active detachment of Taiwan illuminated by small earthquakes and its control of first-order topography, *Geology*, *30*, 935–938.

Champel, B., P. van der Beek, J. Mugnier, and P. Leturmy (2002), Growth and lateral propagation of fault-related folds in the Siwaliks of western Nepal: Rates, mechanisms, and geomorphic signature, *J. Geophys. Res.*, *107*(B6), 2111, doi:10.1029/2001JB000578.

Crosby, B. T., K. X. Whipple, N. M. Gasparini, and C. W. Wobus (2007), Formation of fluvial hanging valleys: Theory and simulation, *J. Geophys. Res.*, *112*, F03S10, doi:10.1029/2006JF000566.

Culling, W. E. H. (1965), Theory of erosion on soil-covered slopes, *J. Geol.*, *73*, 230–254.

De Paor, D. G., and D. J. Anastasio (1987), The Spanish External Sierra: A case history in the advance and retreat of mountains, *Natl. Geogr. Res.*, *3*, 199–209.

Dietrich, W. E., D. G. Bellugi, L. S. Sklar, J. D. Stock, A. M. Heimsath, and J. J. Roering (2003), Geomorphic transport laws for predicting landscape form and dynamics, in *Prediction in Geomorphology*, *Geophys. Monogr.*

Ser., vol. 135, edited by P. R. Wilcock and R. M. Iverson, pp. 103–132, AGU, Washington, D.C.

Duvall, A., E. Kirby, and D. Burbank (2004), Tectonic and lithologic controls on bedrock channel profiles and processes in coastal California, *J. Geophys. Res.*, *109*, F03002, doi:10.1029/2003JF000086.

Ellis, M. A., and A. L. Densmore (2006), First-order topography over blind thrusts, in *Tectonics, Climate, and Landscape Evolution*, edited by S. D. Willett et al., *Spec. Pap. Geol. Soc. Am.*, *398*, 251–266.

England, P. C., and P. Molnar (1990), Surface uplift, uplift of rocks, and exhumation of rocks, *Geology*, *18*, 1173–1177.

Gasparini, N. M., et al. (2006), Numerical modeling of non-steady-state river profile evolution using a sediment-flux-dependent incision model, in *Tectonics, Climate, and Landscape Evolution*, edited by S. D. Willett et al., *Spec. Pap. Geol. Soc. Am.*, *398*, 127–141.

Gasparini, N. M., K. X. Whipple, and R. L. Bras (2007), Predictions of steady state and transient landscape morphology using sediment-flux-dependent river incision models, *J. Geophys. Res.*, *112*, F03S09, doi:10.1029/2006JF000567.

Gilbert, G. K. (1877), *Report on the Geology of the Henry Mountains, Utah*, 160 pp., Gov. Print. Off., Washington, D. C.

Hack, J. T. (1957), Studies of longitudinal stream profiles in Virginia and Maryland, *U.S. Geol. Surv. Prof. Pap.*, *294-B*, 45–97.

Herman, F., and J. Braun (2006), Fluvial response to horizontal shortening and glaciations: A study in the Southern Alps of New Zealand, *J. Geophys. Res.*, *111*, F01008, doi:10.1029/2004JF000248.

Hickman, J. B., et al. (2002), Structure and evolution of the active fold-and-thrust belt of southwestern Taiwan from Global Positioning System analysis, in *Geology and Geophysics of an Arc-Continent Collision, Taiwan*, edited by T. B. Byrne and C.-S. Liu, pp. 75–92, Geol. Soc. of Am., Boulder, Colo.

Hodges, K. V., J. M. Hurtado, and K. X. Whipple (2001), Southward extrusion of Tibetan crust and its effect on Himalayan tectonics, *Tectonics*, *20*(6), 799–809.

Hodges, K. V., et al. (2004), Quaternary deformation, river steepening, and heavy precipitation at the front of the Higher Himalayan ranges, *Earth Planet. Sci. Lett.*, *220*, 379–389.

Howard, A. D., W. E. Dietrich, and M. A. Seidl (1994), Modeling fluvial erosion on regional to continental scales, *J. Geophys. Res.*, *99*, 13,971–13,986.

Hsieh, M.-L., and P. L. K. Knuepfer (2002), Synchroneity and morphology of Holocene river terraces in the southern Western Foothills, Taiwan: A guide to interpreting and correlating erosional river terraces across growing anticlines, in *Geology and Geophysics of an Arc-Continent Collision, Taiwan*, edited by T. B. Byrne and C.-S. Liu, *Spec. Pap. Geol. Soc. Am.*, *358*, 55–74.

Hurtrez, J.-E., F. Lucazeau, J. Lavé, and J.-P. Avouac (1999), Investigation of the relationships between basin morphology, tectonic uplift, and denudation from the study of an active fold belt in the Siwalik Hills, central Nepal, *J. Geophys. Res.*, *104*, 12,779–12,796.

Kirby, E., and K. Whipple (2001), Quantifying differential rock-uplift rates via stream profile analysis, *Geology*, *29*, 415–418.

Koons, P. O. (1990), Two-sided orogen: Collision and erosion from the sandbox to the Southern Alps, New Zealand, *Geology*, *18*, 679–682.

Kuhni, A., and O. A. Pfiffner (2001), Drainage patterns and tectonic forcing: A model study for the Swiss Alps, *Basin Res.*, *13*, 169–197.

Lague, D., and P. Davy (2003), Constraints on the long-term colluvial erosion law by analyzing slope-area relationships at various tectonic uplift rates in the Siwaliks Hills (Nepal), *J. Geophys. Res.*, *108*(B2), 2129, doi:10.1029/2002JB001893.

Lague, D., et al. (2000), Estimating uplift rate and erodibility from the area-slope relationship: Examples from Brittany (France) and numerical modelling, *Phys. Chem. Earth*, *25*, 543–548.

Lavé, J., and J. P. Avouac (2000), Active folding of fluvial terraces across the Siwaliks Hills, Himalayas of central Nepal, *J. Geophys. Res.*, *105*, 5735–5770.

Lavé, J., and J. P. Avouac (2001), Fluvial incision and tectonic uplift across the Himalayas of central Nepal, *J. Geophys. Res.*, *106*, 26,561–526,591.

Leturmy, P., et al. (1995), Erosion et sedimentation au voisinage d'un anticlinal de rampe; apport d'un modele numerique. Erosion and sedimentation in the vicinity of a ramp anticline; contribution of a numerical model, *Bull. Soc. Geol. Fr.*, *166*, 783–795.

Martin, Y. (2000), Modelling hillslope evolution: Linear and nonlinear transport relations, *Geomorphology*, *34*, 1–21.

Martin, Y., and M. Church (1997), Diffusion in landscape development models: On the nature of basic transport relations, *Earth Surf. Processes Landforms*, *22*, 271–279.

McClay, K. R. (Ed.) (2004), *Thrust Tectonics and Hydrocarbon Systems*, 667 pp., Am. Assoc. of Pet. Geol., Tulsa, Okla.

McKean, J. A., et al. (1993), Quantification of soil production and downslope creep rates from cosmogenic ^{10}Be accumulations on a hillslope profile, *Geology*, *21*, 343–346.

Miller, S. R., and R. L. Slingerland (2006), Topographic advection on fault-bend folds: Inheritance of valley positions and the formation of wind gaps, *Geology*, *34*, 769–772.

Moglen, G. E., and R. L. Bras (1995), The effect of spatial heterogeneities on geomorphic expression in a model of basin evolution, *Water Resour. Res.*, *31*, 2613–2623.

Montgomery, D. R. (2002), Valley formation by fluvial and glacial erosion, *Geology*, *30*, 1047–1050.

Montgomery, D. R., and E. Foufoula-Georgiou (1993), Channel network source representation using digital elevation models, *Water Resour. Res.*, *29*, 3925–3934.

Morris, R. G., et al. (1998), Exhumation of the Pyrenean orogen: Implications for sediment discharge, *Basin Res.*, *10*, 69–85.

Mugnier, J.-L., et al. (1999), The Siwaliks of western Nepal; I, Geometry and kinematics, *J. Asian Earth Sci.*, *17*, 629–642.

Mugnier, J.-L., et al. (2004), Episodicity and rates of thrust-sheet motion in the Himalayas (western Nepal), in *Thrust Tectonics and Hydrocarbon Systems*, edited by K. R. McClay, pp. 91–114, Am. Assoc. of Pet. Geol., Tulsa, Okla.

Pazzaglia, F. J., and M. T. Brandon (2001), A fluvial record of long-term steady-state uplift and erosion across the Cascadia forearc high, western Washington State, *Am. J. Sci.*, *301*, 385–431.

Roe, G. H., et al. (2002), Effects of orographic precipitation variations on the concavity of steady-state river profiles, *Geology*, *30*, 143–146.

Roering, J. J., et al. (2002), Soil transport driven by biological processes over millennial time scales, *Geology*, *30*, 1115–1118.

Schlunegger, F., et al. (2001), Climate, exposed source-rock lithologies, crustal uplift and surface erosion: A theoretical analysis calibrated with data from the Alps/North Alpine foreland basin system, *Int. J. Earth Sci.*, *90*, 484–499.

Schoenbohm, L. M., et al. (2004), Geomorphic constraints on surface uplift, exhumation, and plateau growth in the Red River region, Yunnan Province, China, *Geol. Soc. Am. Bull.*, *116*, 895–909.

Seidl, M. A., and W. E. Dietrich (1992), The problem of channel erosion into bedrock, *Catena Suppl.*, *23*, 101–124.

Shaw, J. H., and J. Suppe (1996), Earthquake hazards of active blind-thrust faults under the central Los Angeles Basin, California, *J. Geophys. Res.*, *101*, 8623–8642.

Sklar, L., and W. E. Dietrich (1998), River longitudinal profiles and bedrock incision models: Stream power and the influence of sediment supply, in *Rivers Over Rock: Fluvial Processes in Bedrock Channels*, *Geophys. Monogr. Ser.*, vol. 107, edited by K. Tinkler and E. Wohl, pp. 237–260, AGU, Washington, D. C.

Sklar, L. S., and W. E. Dietrich (2001), Sediment and rock strength controls on river incision into bedrock, *Geology*, *29*, 1087–1090.

Sklar, L. S., and W. E. Dietrich (2004), A mechanistic model for river incision into bedrock by saltating bed load, *Water Resour. Res.*, *40*, W06301, doi:10.1029/2003WR002496.

Smith, R. B. (2006), Progress on the theory of orographic precipitation, in *Tectonics, Climate, and Landscape Evolution*, edited by S. D. Willett et al., *Spec. Pap. Geol. Soc. Am.*, *398*, 1–16.

Snyder, N. P., et al. (2000), Landscape response to tectonic forcing: Digital elevation model analysis of stream profiles in the Mendocino triple junction region, northern California, *Geol. Soc. Am. Bull.*, *112*, 1250–1263.

Stock, J., and W. E. Dietrich (2003), Valley incision by debris flows: Evidence of a topographic signature, *Water Resour. Res.*, *39*(4), 1089, doi:10.1029/2001WR001057.

Stock, J. D., and D. R. Montgomery (1999), Geologic constraints on bedrock river incision using the stream power law, *J. Geophys. Res.*, *104*, 4983–4993.

Stolar, D. B., et al. (2006), Climatic and tectonic forcing of a critical orogen, in *Tectonics, Climate, and Landscape Evolution*, edited by S. D. Willett et al., *Spec. Pap. Geol. Soc. Am.*, *398*, 241–250.

Suppe, J. (1983), Geometry and kinematics of fault-bend folding, *Am. J. Sci.*, *283*, 684–721.

Tomkin, J. H., M. T. Brandon, F. J. Pazzaglia, J. R. Barbour, and S. D. Willett (2003), Quantitative testing of bedrock incision models for the Clearwater River, NW Washington State, *J. Geophys. Res.*, *108*(B6), 2308, doi:10.1029/2001JB000862.

Tucker, G., et al. (2001), The Channel-Hillslope Integrated Landscape Development model (CHILD), in *Landscape Erosion and Evolution Modeling*, edited by R. S. Harmon and W. W. Doe III, pp. 349–388, Kluwer Acad., New York.

Walcott, R. I. (1998), Modes of oblique compression: Late Cenozoic tectonics of the South Island of New Zealand, *Rev. Geophys.*, *36*, 1–26.

Wellman, H. W. (1979), An uplift map for the South Island of New Zealand, and a model for uplift of the Southern Alps, *Bull. R. Soc. N. Z.*, *18*, 13–20.
Wesnousky, S. G., S. Kumar, R. Mohindra, and V. C. Thakur (1999), Uplift and convergence along the Himalayan Frontal Thrust of India, *Tectonics*, *18*(6), 967–976.
Whipple, K. X. (2004), Bedrock rivers and the geomorphology of active orogens, *Annu. Rev. Earth Planet. Sci.*, *32*, 151–185.
Whipple, K. X., and B. J. Meade (2004), Controls on the strength of coupling among climate, erosion, and deformation in two-sided, frictional orogenic wedges at steady state, *J. Geophys. Res.*, *109*, F01011, doi:10.1029/2003JF000019.
Whipple, K. X., and G. E. Tucker (1999), Dynamics of the stream-power river incision model: Implications for height limits of mountain ranges, landscape response timescales, and research needs, *J. Geophys. Res.*, *104*, 17,661–17,674.
Whipple, K. X., and G. E. Tucker (2002), Implications of sediment-flux-dependent river incision models for landscape evolution, *J. Geophys. Res.*, *107*(B2), 2039, doi:10.1029/2000JB000044.
Willett, S. D. (1999), Orogeny and orography: The effects of erosion on the structure of mountain belts, *J. Geophys. Res.*, *104*, 28,957–28,982.
Willett, S. D., and M. T. Brandon (2002), On steady states in mountain belts, *Geology*, *30*, 175–178.
Willett, S., et al. (1993), Mechanical model for the tectonics of doubly vergent compressional orogens, *Geology*, *21*, 371–374.
Willett, S. D., et al. (2001), Uplift, shortening, and steady state topography in active mountain belts, *Am. J. Sci.*, *301*, 455–485.
Willett, S. D., et al. (2003), Erosion rates and orogenic-wedge kinematics in Taiwan inferred from fission-track thermochronometry, *Geology*, *31*, 945–948.
Willett, S. D., et al. (Eds.) (2006), *Tectonics, Climate, and Landscape Evolution*, *Spec. Pap. Geol. Soc. Am.*, vol. 398, Geol. Soc. of Am., Boulder, Colo.
Wobus, C. W., et al. (2003), Has focused denudation sustained active thrusting at the Himalayan topographic front?, *Geology*, *31*, 861–864.
Wobus, C., et al. (2006a), Tectonics from topography: Procedures, promise, and pitfalls, in *Tectonics, Climate, and Landscape Evolution*, edited by S. D. Willett et al., *Spec. Pap. Geol. Soc. Am.*, *398*, 55–74.
Wobus, C. W., B. T. Crosby, and K. X. Whipple (2006b), Hanging valleys in fluvial systems: Controls on occurrence and implications for landscape evolution, *J. Geophys. Res.*, *111*, F02017, doi:10.1029/2005JF000406.

E. Kirby, S. R. Miller, and R. L. Slingerland, Department of Geosciences, Pennsylvania State University, University Park, PA 16802, USA. (srmiller@geosc.psu.edu)